Title	Analyzing and Quantifying the Gain-of-Function Enhancement of IP3 Receptor Gating by Familial Alzheimer's Disease-Causing Mutants in Presenilins
Author(s)	Mak, DD; Cheung, KH; Toglia, P; Foskett, JK; Ullah, G
Citation	PLoS Computational Biology, 2015, v. 11 n. 10, p. e1004529
Issued Date	2015
URL	http://hdl.handle.net/10722/224850
Rights	This work is licensed under a Creative Commons Attribution-NonCommercial-NoDerivatives 4.0 International License.

Analyzing and Quantifying the Gain-of-Function Enhancement of IP$_3$ Receptor Gating by Familial Alzheimer's Disease-Causing Mutants in Presenilins

Don-On Daniel Mak[1], King-Ho Cheung[2], Patrick Toglia[3], J. Kevin Foskett[1,4], Ghanim Ullah[3]*

1 Department of Physiology, University of Pennsylvania, Philadelphia, Pennsylvania, United States of America, 2 Department of Physiology, The University of Hong Kong, Pok Fu Lam, Hong Kong, 3 Department of Physics, University of South Florida, Tampa, Florida, United States of America, 4 Department of Cell and Developmental Biology, University of Pennsylvania, Philadelphia, Pennsylvania, United States of America

* gullah@usf.edu

Abstract

Familial Alzheimer's disease (FAD)-causing mutant presenilins (PS) interact with inositol 1,4,5-trisphosphate (IP$_3$) receptor (IP$_3$R) Ca^{2+} release channels resulting in enhanced IP$_3$R channel gating in an amyloid beta (Aβ) production-independent manner. This gain-of-function enhancement of IP$_3$R activity is considered to be the main reason behind the upregulation of intracellular Ca^{2+} signaling in the presence of optimal and suboptimal stimuli and spontaneous Ca^{2+} signals observed in cells expressing mutant PS. In this paper, we employed computational modeling of single IP$_3$R channel activity records obtained under optimal Ca^{2+} and multiple IP$_3$ concentrations to gain deeper insights into the enhancement of IP$_3$R function. We found that in addition to the high occupancy of the high-activity (H) mode and the low occupancy of the low-activity (L) mode, IP$_3$R in FAD-causing mutant PS-expressing cells exhibits significantly longer mean life-time for the H mode and shorter life-time for the L mode, leading to shorter mean close-time and hence high open probability of the channel in comparison to IP$_3$R in cells expressing wild-type PS. The model is then used to extrapolate the behavior of the channel to a wide range of IP$_3$ and Ca^{2+} concentrations and quantify the sensitivity of IP$_3$R to its two ligands. We show that the gain-of-function enhancement is sensitive to both IP$_3$ and Ca^{2+} and that very small amount of IP$_3$ is required to stimulate IP$_3$R channels in the presence of FAD-causing mutant PS to the same level of activity as channels in control cells stimulated by significantly higher IP$_3$ concentrations. We further demonstrate with simulations that the relatively longer time spent by IP$_3$R in the H mode leads to the observed higher frequency of local Ca^{2+} signals, which can account for the more frequent global Ca^{2+} signals observed, while the enhanced activity of the channel at extremely low ligand concentrations will lead to spontaneous Ca^{2+} signals in cells expressing FAD-causing mutant PS.

Author Summary

Aberrant Ca^{2+} signaling caused by IP$_3$R gating dysregulation is implicated in many neurodegenerative diseases such as Alzheimer's, Huntington's, Spinocerebellar ataxias, and endoplasmic reticulum stress-induced brain damage. Thus understanding IP$_3$R dysfunction is important for the etiology of these diseases. It was previously shown that FAD-causing mutant PS interacts with the IP$_3$R, leading to its gain-of-function enhancement in optimal Ca^{2+} and sub-saturating IP$_3$ concentrations. Here, we use data-driven modeling to provide deeper insights into the upregulation of IP$_3$R gating in a wide range of ligand concentrations and quantify the sensitivity of the channel to its ligands in the presence of mutant PS. Our simulations demonstrate that these changes can alter the statistics of local Ca^{2+} events and we speculate that they lead to Ca^{2+} signaling dysregulations at the whole cell level observed in FAD cells. These models will provide the foundation for future data-driven computational framework for local and global Ca^{2+} signals that will be used to judiciously isolate the primary pathways causing Ca^{2+} dysregulation in FAD from those that are downstream, and to study the effects of upregulation of IP$_3$R activity on cell function.

Introduction

Alzheimer's disease (AD) is a fatal neurodegenerative disease that leads to cognitive, memory, and behavioral impairments followed by progressive cell death. The symptoms of AD include the extracellular deposition of amyloid β (Aβ) plaques and intracellular neurofibrillary tangles —aggregates of microtubule-associated protein τ [1]. According to the amyloid hypothesis, the accumulation of Aβ oligomers or plaques due to the imbalance between synthesis and clearance of Aβ is the driving force for AD pathogenesis [2]. However, whether τ and Aβ aggregates are the causes or symptoms of AD remains a matter of debate [3].

Aβ is produced by the cleavage of amyloid precursor protein (APP), an integral membrane protein. APP is cleaved sequentially by β and γ-secretases to generate Aβ monomers that are released to the extracellular space and form oligomers. The γ-secretase complex contains four different proteins including presenilins (PS) that are synthesized and localized in the ER [1]. Mutations in PS alter the APP processing, thus leading to Aβ oligomarization either through higher production or relatively higher proportion of amyloidogenic Aβ types [4]. It is well established that mutations in PS and APP are the main causes of Familial AD (FAD) [5]. What is not clear is how PS mutations and Aβ accumulation lead to the impairment of brain function and neurodegeneration. The Ca^{2+} hypothesis of AD, which is based on the enhanced intracellular Ca^{2+} signaling during AD, accounts for early memory loss and subsequent cell death [6, 7, 8].

There is strong evidence in favor of intracellular Ca^{2+} signal exaggeration by FAD-causing PS mutations as an early phenotype that could contribute to the pathogenesis of the disease [9]. The exaggerated cytosolic Ca^{2+} signals are ascribed mainly to the enhanced release of Ca^{2+} from intracellular endoplasmic reticulum (ER) store due to overloading of ER lumen by up-regulated sarco-endoplasmic reticulum Ca^{2+}-ATPase (SERCA) pump [10]; disruption of ER-membrane Ca^{2+} leak channels [11]; or enhanced gating of IP$_3$R [12, 13, 14, 15], the ubiquitous ER-localized Ca^{2+} release channel crucial for the generation and modulation of intracellular Ca^{2+} signals in animal cells [16]. Single channel studies in multiple cell lines show that the sensitivity of IP$_3$R to its agonist IP$_3$ increases significantly in the presence of FAD-causing mutant PS [14, 15], leading to a several fold increase in the open probability (P_o) of IP$_3$R channel in subsaturating IP$_3$. These studies were performed in the absence of Aβ, suggesting that the modulation of IP$_3$R is a major mechanism for intracellular Ca^{2+} signal dysregulation in cells

expressing FAD-causing mutant PS. Furthermore, altered IP$_3$R-mediated Ca^{2+} release has been suggested as the fundamental defect and highly predictive diagnostic feature in AD [17]. Suppression of IP$_3$R-mediated Ca^{2+} signaling was recently shown to restore normal cell function and memory tasks in M146V (FAD-causing PS mutation) knock-in [18] and triple-transgenic [19] mice models of FAD [20].

IP$_3$R gates in three distinct modes: an "L" mode with very low P_o, in which brief openings are separated by quiescent periods with long mean closed channel durations (τ_c); an "I" mode with intermediate P_o, in which the channel opens and closes rapidly with short τ_c and mean open channel durations (τ_o); and an "H" mode with high P_o, in which the channel gates in bursts [21]. All three modes are observed under all conditions in which the channel gates, and the channel spontaneously switches among all three modes even under constant ligand conditions. The P_o of the channel remains remarkably consistent in each gating mode in all ligand conditions so the ligand dependencies of overall channel P_o, τ_o and τ_c come from the ligand dependencies of the relative prevalence (normalized occupancy) π^M of the gating modes (M can be L, I, and H) [21].

Due to the significant role of IP$_3$R-mediated Ca^{2+} signaling dysregulation in AD, a comprehensive understanding of the IP$_3$R function is important for both the etiology of the disease and designing effective therapeutic reagents. It was discovered that IP$_3$R channels in cells expressing FAD-causing mutant PS exhibit relatively higher π^H and lower π^L in comparison to IP$_3$R in cells expressing wild-type PS [15, 14] in non-optimal ligand conditions. π^I, on the other hand, remains largely the same. The switch in the prevalence of H and L modes causes the increase in P_o of IP$_3$R in the presence of FAD-causing mutant PS.

In this paper, we employ a data-driven modeling approach to gain further insights into the gating behavior of IP$_3$R in the presence of wild-type and FAD-causing PS. We focus on the channel gating behaviors of endogenous IP$_3$R in the presence of human wild-type (PS1-WT) and FAD-causing mutant (PS1-M146L) PS expressed in the Sf9 cells, an insect cell line derived from the moth Spodoptera frugiperda. Other FAD-causing mutant PS1 (PS1-L116P, PS1-G384A) and PS2 (PS2-N141I) have similar effects on IP$_3$R channel gating as PS1-M146L. On the other hand, non-FAD-associated mutant PS1 (PS1-L113P and PS1-G183V), wild-type PS2 and EVER1 (an irrelevant ER transmembrane protein) have little to no effects on IP$_3$R channel gating, like PS1-WT [15, 14]. Therefore, the conclusions from studying IP$_3$R channel in the presence of PS1-WT (IP$_3$R$_{PS1WT}$) and IP$_3$R channel in the presence of PS1-M146L (IP$_3$R$_{PS1M146L}$) can be generalized to other FAD-causing mutations as well. We used the data-driven kinetic model developed to describe *all* observed gating behaviors of the endogenous IP$_3$R channels in Sf9 cells: channel P_o, τ_o and τ_c distributions in various steady Ca^{2+} and IP$_3$ concentrations ($\mathcal{C}$ and $\mathcal{I}$, respectively); modal gating behaviors in various steady $\mathcal{C}$ and $\mathcal{I}$; and kinetic response of IP$_3$R channels to abrupt changes in $\mathcal{I}$ and/or $\mathcal{C}$ [22] as the starting point of our approach. By modifying a minimum number of model parameters, the data-driven model was applied to fit observed gating behaviors: channel P_o, τ_o, τ_c, and modal prevalence, in optimal (1 μM) $\mathcal{C}$ and sub-saturating (100 nM) $\mathcal{I}$, of the Sf9 IP$_3$R$_{PS1M146L}$ and IP$_3$R$_{PS1WT}$ (used as control) [15] as well as P_o, τ_o, and τ_c of IP$_3$R$_{PS1WT}$ in 33 nM and 10μM $\mathcal{I}$ at $\mathcal{C}$ = 1μM. In addition to elucidating the kinetics and factors contributing to the gain-of-function enhancement of IP$_3$R activity [14, 15], we extrapolate, using our modified model, the gating behavior of IP$_3$R$_{PS1WT}$ and IP$_3$R$_{PS1M146L}$ for a wide range of $\mathcal{C}$ and $\mathcal{I}$. We also quantify and compare the ligand sensitivities of IP$_3$R$_{PS1M146L}$ and IP$_3$R$_{PS1WT}$. Simulations of local Ca^{2+}-release events based on the results of the data-driven model demonstrate that the gain-of-function enhancement of IP$_3$R activity leads to larger, longer, and more frequent local Ca^{2+} releases events in cells expressing FAD-causing PS mutants. The models derived here will provide the foundation for developing future data-driven computational framework for global intracellular Ca^{2+}

signals that will be used to judiciously isolate the primary factors causing Ca^{2+} signaling dysregulation in FAD from those that are downstream, and to study the effects of upregulation of IP$_3$R activity on cell functions such as ATP production.

Materials and Methods

Experimental Methods

The main experimental data used in this paper for fitting the models were previously published elsewhere [15]. Basic experimental data (P_o, τ_o, and τ_c) at $\mathcal{I}$ = 33nM, and 10μM for both IP$_3$R$_{PS1WT}$ and IP$_3$R$_{PS1M146L}$ [14] were also used to generate our model. The full details of experimental methods are given in [15] and summarized below.

Two Sf9 cell lines expressing recombinant PS1-WT and PS1-M146L, respectively, were generated and maintained as described in [14].

Nuclei isolated from transfected Sf9 cells [23, 14] were used for nuclear patch clamp experiments in on-nucleus configuration at room temperature [24]. All experimental solutions contained 140 mM KCl and 10 mM HEPES (pH 7.3). Bath solution contained 90 nM free Ca^{2+} (buffered by 0.5 mM BAPTA (1,2-bis(2-aminophenoxy)ethane-N,N,N',N'-tetraacetic acid). Pipette solution contained 1 μM free Ca^{2+} (buffered by 0.5 mM 5,5'-dibromo-BAPTA), 0.5 mM Na$_{2ATP}$ and sub-saturating 100 nM IP$_3$.

Segments of current records exhibiting current levels for a single IP$_3$R channel were idealized with QuB software (University of Buffalo) using SKM algorithm [25, 26]. The idealized current traces were further analyzed as described in [21] to characterized the modal gating behaviors of IP$_3$R channels. Short closing events, presumably caused by ligand-independent transitions [27], were removed by burst analysis. Gating modes were assigned according to durations of channel burst (T$_b$) and burst-terminating gaps (T$_g$) [21], using a critical T$_b$ of 100 ms and a critical T$_g$ of 200 ms to detect modal transitions.

Computational Methods

We fit the twelve-state model previously developed for IP$_3$R in Sf9 cells [22] (Fig 1) to the channel gating data of Sf9 IP$_3$R$_{PS1WT}$ and IP$_3$R$_{PS1M146L}$ at $\mathcal{C}$ = 1μM and $\mathcal{I}$ = 100 nM [15], following the procedure in [22, 28, 29], which we describe below. Although the scheme in Fig 1 seems to suggest simultaneous binding/unbinding of multiple ligands as the channel goes from one state to another (for instance C$_{00}^L$ to C$_{20}^L$, or C$_{24}^H$ to C$_{20}^L$), in reality, there is no such direct transition in our model. Each one of such transitions actually involves one or more intermediate states that are not explicitly shown in order to keep the scheme simple. As discussed in detail in [22], the simplifying approximations were made by considering the fact that the intermediate states have relatively low occupancy and therefore can be aggregated into the main states. The rates for the composite transitions between those main states explicitly shown in the scheme were actually derived with the intermediate low-occupancy states carefully taken into consideration.

Occupancy parameters.   First, we derive the optimal parameters specifying the occupancy of various gating states from the mean P_o and prevalences of the three modes.

Open Probability: In the following, C$_{mn}^M$ and O$_{mn}^M$ represent a closed and open state respectively in the M mode (where M = L, I, or H) with m Ca^{2+} and n IP$_3$ bound to the channel. Relative to the reference unliganded closed state C$_{00}^L$, the occupancies of C$_{mn}^M$ and O$_{mn}^M$ states are proportional to $\mathcal{C}^m \mathcal{I}^n$, with occupancy parameters $K_{C_{mn}^M}$ and $K_{O_{mn}^M}$, respectively. The occupancy parameter of a state is equal to the product of equilibrium association constants along any path connecting C$_{00}^L$ to that state ($K_{C_{00}^L} = 1$). The normalized occupancy of C$_{mn}$ and O$_{mn}$ are $K_{C_{mn}^M} \mathcal{C}^m \mathcal{I}^n / Z$ and $K_{O_{mn}^M} \mathcal{C}^m \mathcal{I}^n / Z$, respectively, where Z, the total occupancy of all states, is
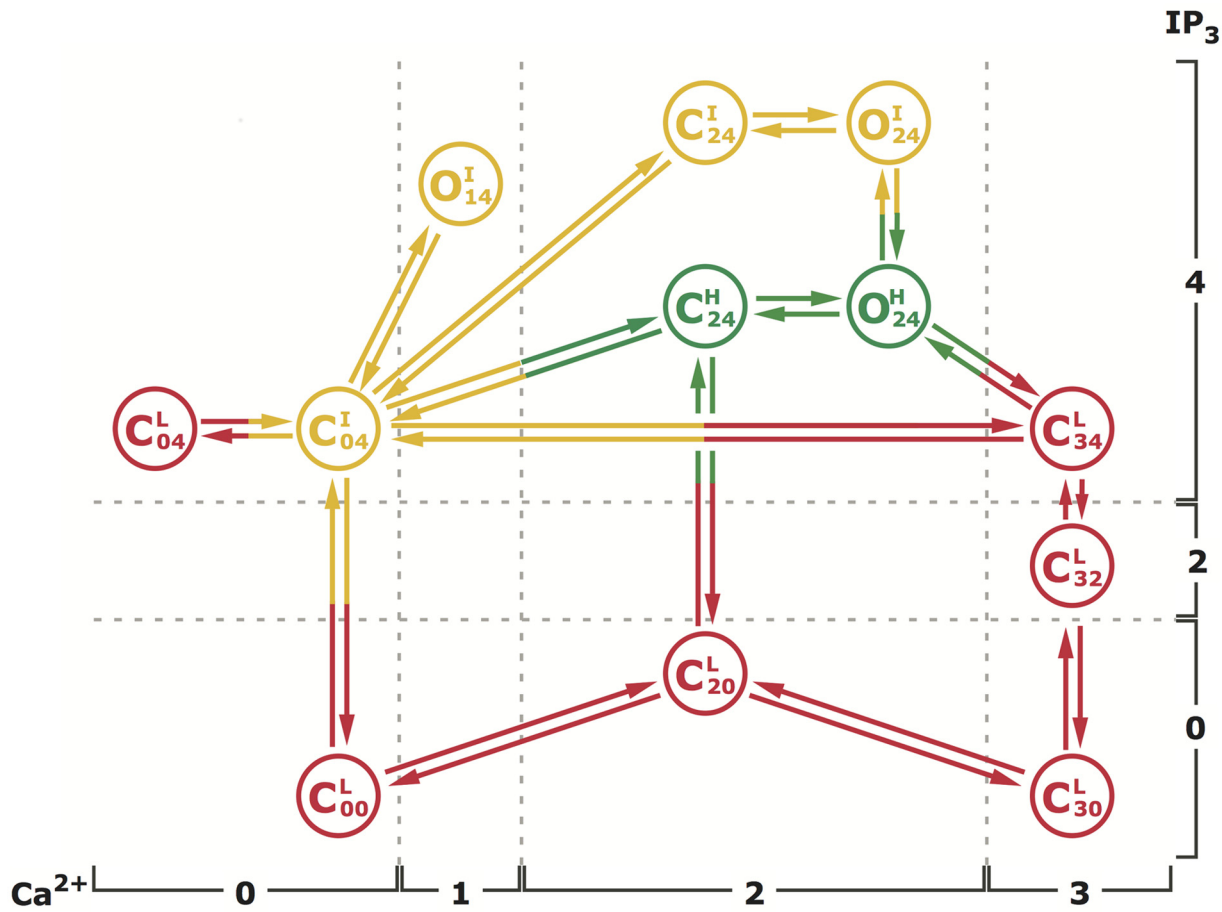
Fig 1. The kinetic scheme for the proposed model. The superscript of each state denote the gating mode that state is in. The two numbers in the subscripts respectively indicate the number of Ca^{2+} and IP_3 bound to the channel in that state. The model has nine closed states: C_{00}^L, C_{20}^L, C_{30}^L, C_{32}^L, C_{34}^L, C_{04}^L, C_{04}^I, C_{24}^I, and C_{24}^H and three open states: O_{14}^I, O_{24}^I, and O_{24}^H. The transition rates between various states and the related flux parameters are listed in Tables [2] and [3] respectively.

given by

$$Z = \{Z_o\} + \{Z_c\} = \{K_{O_{14}^I}\mathcal{C}\mathcal{I}^4 + K_{O_{24}^I}\mathcal{C}^2\mathcal{I}^4 + K_{O_{24}^H}\mathcal{C}^2\mathcal{I}^4\}$$
$$+ \{K_{C_{00}^L} + K_{C_{20}^L}\mathcal{C}^2 + K_{C_{30}^L}\mathcal{C}^3 + K_{C_{32}^L}\mathcal{C}^3\mathcal{I}^2 + K_{C_{34}^L}\mathcal{C}^3\mathcal{I}^4 \quad (1)$$
$$+ K_{C_{04}^L}\mathcal{I}^4 + K_{C_{04}^I}\mathcal{I}^4 + K_{C_{24}^I}\mathcal{C}^2\mathcal{I}^4 + K_{C_{24}^H}\mathcal{C}^2\mathcal{I}^4 \}.$$

The equilibrium P_o function is:

$$P_o(\mathcal{C}, \mathcal{I}) = \frac{Z_o}{Z} \quad . \quad (2)$$

Modal Prevelances: The IP₃R channel exhibits three distinct gating modes [21]. The relative prevalence, π^M, of the gating mode [21] is given as

$$\pi^M = Z^M/Z, \quad (3)$$

where Z^{M} is the sum of occupancies of all states in a given mode. For example, for H mode, Z^{H} = $K_{C_{24}^{\text{H}}}\mathcal{C}^2\mathcal{I}^4 + K_{O_{24}^{\text{H}}}\mathcal{C}^2\mathcal{I}^4$.

We fit P_o π^{L}, π^{I}, and π^{H} function simultaneously to the P_o and prevalence data using the Mathematica routine "NonlinearModelFit" based on least squares fitting. We perform this fit for single channel data from both IP$_3$R$_{\text{PS1WT}}$ and IP$_3$R$_{\text{PS1M146L}}$ to get the optimal occupancy parameters for IP$_3$R in the presence of wild-type and FAD-causing mutant PS.

Probability flux parameters. To determine the parameters describing the probability flux between different model states [22] involved in the transition rates between various states, we performed maximum likelihood fits on current traces of channel gating from IP$_3$R$_{\text{PS1WT}}$ and IP$_3$R$_{\text{PS1M146L}}$.

Maximum Likelihood and AIC Calculations: We calculated the "log-likelihood" function for the model in the open-source programming language "Octave" and used the function "nelder_-mead_min" in the optimization tool kit to minimize the likelihood score ($-log(likelihood(data))$) of the time-series data by varying the 18 free flux parameters while holding the occupancy parameters fixed. The log of the likelihood function for the current traces is given as [30]

$$
\begin{aligned}
log(likelihood(tc_1, to_1, tc_2, to_2, \ldots tc_n, to_n)) \ = \ & log(\pi_C exp(Q_{CC}tc_1)Q_{CO}exp(Q_{OO}to_1) \\
& Q_{OC}exp(Q_{CC}tc_2)Q_{CO}exp(Q_{OO}to_2)\ldots \\
& exp(Q_{OO}to_n)u_O),
\end{aligned} \tag{4}
$$

where π_C is the initial probability of closed states being occupied at equilibrium, to_i and tc_i are the ith opening and closing in the time-series respectively, and Q_{CC}, Q_{OO}, Q_{OC}, and Q_{CO} are the sub-matrices of the 12×12 generator matrix Q. That is,

$$
Q = \begin{pmatrix} Q_{OO} & Q_{OC} \\ Q_{CO} & Q_{CC} \end{pmatrix}. \tag{5}
$$

The element of Q at location ij, $Q_{ij}, i \neq j$ is the transition rate from state i to state j. The diagonal entries are given by $Q_{ii} = -\Sigma_{j \neq i} Q_{ij}$, which is an expression of conservation of probability [31]. Thus Q_{CC}, Q_{OO}, Q_{OC}, and Q_{CO} are matrices of the transition rates from all closed to all closed, all open to all open, all open to all closed, and all closed to all open states, respectively. Since our model has 9 closed and 3 open states, Q_{CC}, Q_{OO}, Q_{CO}, and Q_{OC} are 9×9, 3×3, 9×3, and 3×9 matrices respectively. For data obtained at equilibrium, $\pi_C = W_O Q_{OC}/J$, with $J = W_O Q_{OC} u_C$, where u_C is a nine—(the number of close states) component vector of all 1's. W_C and W_O are diagonal matrices of the equilibrium occupancies of all closed and all open states respectively.

The total log-likelihood of all data used in the fit was calculated as

$$
log(likelihood(data)) = \sum_{i=1}^{N_{exp}} log(likelihood(data_i)), \tag{6}
$$

where N_{exp} is the number of experiments and $data_i$ is the data set (time series) from experiment i. A total of 30 and 15 experiments were used in the global fit for the IP$_3$R gating in the presence of PS1-WT and PS1-M146L, respectively.

Mean open and closed times. The mean open and closed times are given by

$$
\begin{aligned}
\tau_o \ &= \ P_o(\mathcal{C}, \mathcal{I})/J \\
\tau_c \ &= \ (1 - P_o(\mathcal{C}, \mathcal{I}))/J,
\end{aligned} \tag{7}
$$

where J is the total equilibrium flux from the 3 open states to the closed states. The equilibrium flux from a given state to other states is the product of the occupancy of that state and the sum

of transition rates from that state to others. Thus, J is given as [22]:

$$
\begin{aligned}
J \quad = \quad & K_{O_{24}^H} \mathcal{C}^2 \mathcal{I}^4 \times \left(r_{(O_{24}^H \to C_{24}^H)} + r_{(O_{24}^H \to C_{34}^L)} \right) \\
& + K_{O_{24}^I} \mathcal{C}^2 \mathcal{I}^4 \times r_{(O_{14}^I \to C_{24}^I)} \\
& + K_{O_{14}^I} \mathcal{C} \mathcal{I}^4 \times r_{(O_{14}^I \to C_{04}^I)},
\end{aligned}
\tag{8}
$$

where $r_{(S \to U)}$ is the transition rate from state S to state U.

Mean modal lifetimes. The lifetime τ^X of any aggregate X (mode or other combinations of Markovian states), in an aggregated Markov chain is given by

$$
\tau^X = \frac{Z^X}{J_X},
\tag{9}
$$

where Z^X is the unnormalized occupancy of aggregate X and J_X the unnormalized flux out of that aggregate. J_X is the sum of all the fluxes from all reactions from all Markovian states contained in the aggregate X to Markovian states not contained in X, so $J_X = \Sigma_S J_S = \Sigma_S(Z_S \Sigma_U r_{(S \to U)})$, where Σ_S is summing over all Markovian states S in the aggregate X, Σ_U is summing over all Markovian states U that are *not* in X. For example for H mode, $\tau^H = \frac{Z^H}{J_H}$, where $Z^H = K_{C_{24}^H} \mathcal{C}^2 \mathcal{I}^4 + K_{O_{24}^H} \mathcal{C}^2 \mathcal{I}^4$ and $J_H = K_{O_{24}^H} \mathcal{C}^2 \mathcal{I}^4 \left(r_{(O_{24}^H \to C_{34}^L)} + r_{(O_{24}^H \to O_{24}^I)} \right) + K_{C_{24}^H} \mathcal{C}^2 \mathcal{I}^4 \left(r_{(C_{24}^H \to C_{04}^I)} + r_{(C_{24}^H \to C_{20}^L)} \right)$.

Dwell-time distributions. In the following, we first derive the expressions for the open and closed dwell-time distributions and later generalize them for the dwell-time distributions in any aggregate of states. We define a 12×12 diagonal matrix W with W_{ii} equal to the equilibrium occupancy of ith state. We partition the W matrix into W_C and W_O, where W_C and W_O are diagonal matrices of the equilibrium occupancies of the 9 closed states and 3 open states respectively in the model. The open time distribution is the probability density for a channel that opened at time 0 to close for the first time at t_O. The probability that the channel first closed at time t_O is given by

$$
\frac{dp_O}{dt} = p_O Q_{OO}.
\tag{10}
$$

which has solution $p_o(t_o) = \pi_O \, exp(Q_{OO} \, t_O)$. The probability, F_O, that the channel remains open at time t_O is the sum of the probability over all the open states and is given as

$$
F_O(t_O) = \pi_O exp(Q_{OO} t_O) u_O,
\tag{11}
$$

where u_O and u_C are column vectors of all ones having dimensions equal to the number of open and close states respectively. The probability, G_C, that the channel closes for the first time at time t_O is $G_C(t_O) = 1 - F_O(t_O)$. The open dwell-time distribution, $f_O(t_O)$ is defined by [32, 33, 30, 31]:

$$
\int_0^{t_O} f_O(t) dt = G_C(t_O),
\tag{12}
$$

or $f_O(t_O) = dG_C(t_O)/dt_O$ so that

$$
f_O(t_O) = -\pi_O exp(Q_{OO} t_O) Q_{OO} u_O,
\tag{13}
$$

which can be written as

$$
f_O(t_O) = \pi_O exp(Q_{OO} t_O) Q_{OC} u_C.
\tag{14}
$$

Similarly, the closed time distribution is given as

$$f_C(t_C) = \pi_C exp(Q_{CC}t_C)Q_{CO}u_O. \tag{15}$$

The initial probabilities of open and closed states being occupied at equilibrium are given as

$$\pi_O = \frac{W_C Q_{CO}}{J} \tag{16}$$

$$\pi_C = \frac{W_O Q_{OC}}{J}, \tag{17}$$

where $J = W_C Q_{CO} u_O = W_O Q_{OC} u_C$ is the total flux from all open states to all closed states at equilibrium and vice versa.

Generalizing this result, the dwell-time distributions of aggregates X and Y respectively are given as

$$f_X(t_X) = \pi_X exp(Q_{XX}t_X)Q_{XY}u_Y. \tag{18}$$

Similarly, the closed time distribution is given as

$$f_Y(t_Y) = \pi_Y exp(Q_{YY}t_Y)Q_{YX}u_X. \tag{19}$$

The initial probabilities of states in X and Y being occupied at equilibrium are given as

$$\pi_X = \frac{W_Y Q_{YX}}{J} \tag{20}$$

$$\pi_Y = \frac{W_X Q_{XY}}{J}, \tag{21}$$

where $J = W_Y Q_{YX} u_X = W_X Q_{XY} u_Y$.

For the open and close dwell-time distributions in a given mode, X and Y consist of all open and close states in the mode respectively. Thus, $X = [O_{24}^I, O_{14}^I]$, $Y = [C_{24}^I, C_{04}^I]$ for I mode and $X = [O_{24}^H]$, $Y = [C_{24}^H]$ for H mode. W_Y and W_X are diagonal matrices of the equilibrium occupancies of all closed states and all open states in the given mode respectively. u_X and u_Y are column vectors of all ones having dimensions equal to the number of open and close states respectively in the mode. The square matrix Q has the dimensions of the number of states in the mode (4 for I mode, 2 for H mode). Sub-matrices Q_{XY} of Q has the transition rates from all states in X to all states in Y aggregate in the mode etc. For example for I mode,

$$Q_{XX} = \begin{pmatrix} -r_{(O_{14}^I \to C_{04}^I)} & 0 \\ 0 & -r_{(O_{24}^I \to C_{24}^H)} \end{pmatrix} \tag{22}$$

$$Q_{XY} = \begin{pmatrix} r_{(O_{14}^I \to C_{04}^I)} & 0 \\ 0 & r_{(O_{24}^I \to C_{24}^I)} \end{pmatrix} \tag{23}$$

$$Q_{YX} = \begin{pmatrix} r_{(C_{04}^I \to O_{14}^I)} & 0 \\ 0 & r_{(C_{24}^I \to O_{24}^I)} \end{pmatrix} \tag{24}$$

$$Q_{YY} = \begin{pmatrix} -r_{(C_{04}^I \to O_{14}^I)} - r_{(C_{04}^I \to C_{24}^I)} & r_{(C_{04}^I \to C_{24}^I)} \\ r_{(C_{24}^I \to C_{04}^I)} & -r_{(C_{24}^I \to O_{24}^I)} - r_{(C_{24}^I \to C_{04}^I)} \end{pmatrix} \tag{25}$$

Similar matrices can be written for H mode where each sub-matrix is of dimension one (one close and one open state each in X and Y).

Stochastic simulations of an IP₃R cluster. To simulate Ca^{2+} puffs and blips (local Ca^{2+} release events from the ER due to nearly simultaneous opening of multiple channels and a single channel, respectively, in a cluster of several IP₃R channels), we followed a procedure developed in [28] and consider a cluster of ten IP₃R channels arranged in a two dimensional array with an inter-channel spacing of 120 nm. The gating of each channel is given by the twelve-state model shown in Fig 1.

Ca^{2+} concentration on the cytoplasmic side of the cluster is controlled by diffusion; the flux coming out from the ER through IP₃R channels, J_j; and the concentration of free dye, b_d. Thus the rate equations for the concentrations of free Ca^{2+} $c^j(r_j, t)$ and free Ca^{2+} dye buffer $b_d^j(r_j, t)$ at distance r_j from channel j and time t are described as below:

$$\frac{\partial c^j(r_j, t)}{\partial t} = D_c \nabla_j^2 c_j + J_j \delta(r_j) + k_d^r(B_d - b_d^j) - k_d^f c^j b_d^j \tag{26}$$

$$\frac{\partial b_d^j}{\partial t} = D_d \nabla_j^2 b_d^j + k_d^r(B_d - b_d^j) - k_d^f c^j b_d^j. \tag{27}$$

In the above equations, B_d is the total concentration, k_d^f the forward (binding) rate, and k_d^r the reverse (unbinding) rate for dye buffer. D_c and D_d are the diffusion coefficients for Ca^{2+} and dye respectively. $\delta(r_j)$ is the Dirac delta function and J_j is the Ca^{2+} flux through the jth channel.

$$J_j = \begin{cases} \frac{I}{2 \times F \times \delta V} & \text{for } r \leq \Delta r, \\ 0 & \text{for } r > 0. \end{cases} \tag{28}$$

Where $I = 0.05$ pA is the channel current, F is the Faraday's constant, $\Delta r = 2.5 nm$, and δV is the volume of the hemisphere over the channel having a radius of r_{pore} [34]. We assume that the Ca^{2+} pump and leak currents are slow on the time scales considered here and therefore have negligible effects. Various parameters used in Eqs (26) and (27) are given in S1 Text.

The propagation of Ca^{2+} and dye is simulated throughout a 3D cytosolic space. Considering the spherical symmetry around the channel, the Laplacian of Ca^{2+} and buffers in spherical coordinates is given as

$$\nabla_j^2 X(r_j, t) = \frac{1}{r_j^2} \frac{\partial}{\partial r_j} \left(r_j^2 \frac{\partial X}{\partial r_j} \right) \tag{29}$$

where $X = c^j$, or b_d^j.

We solved the two differential equations Eqs (26) and (27) using an implicit numerical method based on finite differences for discretizing the system of PDEs on a hemispherical volume of radius 5 μm with a spatial grid size of 5 nm for each channel as described in the S1 Text and summed the contribution of all channels for the instantaneous Ca^{2+} concentration at a given point in space. The Ca^{2+} concentration at the location of each channel is updated by
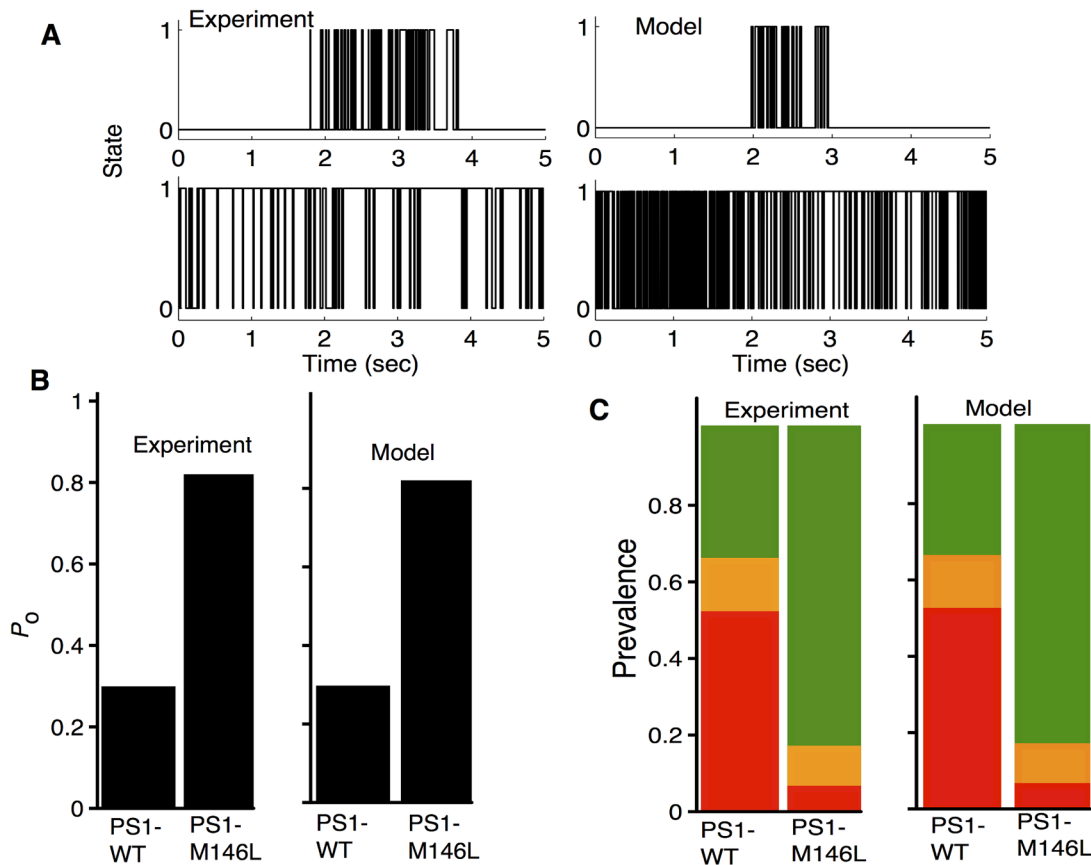
Fig 2. Effect of PS1-WT and PS1-M146L on the gating of IP₃R. (A) Representative idealized experimental (left) and model-simulated (right) time-traces for IP₃R$_{PS1WT}$ (top) and IP₃R$_{PS1M146L}$ (bottom) at $\mathcal{C} = 1\mu M$ and $\mathcal{I} = 100nM$, where 0 and 1 represent closed and open states, respectively. (B and C) Experimental (left) and model-simulated (right) P_o and π^M, respectively, of IP₃R channels in the presence of PS1-WT and PS1-M146L. In (C), relative prevalence of the L, I, and H modes are in red, orange and green, respectively.

doi:10.1371/journal.pcbi.1004529.g002

adding the contributions from other channels in the cluster

$$\mathcal{C}_i = \sum_{j=1}^{10} c^j(r_{ij}) \tag{30}$$

Where r_{ji} is the distance between channels i and j.

Results

Representative time-series traces of the gating behavior of IP₃R$_{PS1WT}$ and IP₃R$_{PS1M146L}$ are shown in Fig 2A. Occupancy parameters for the twelve states in the model obtained by fitting the P_o (Figs 2B, 3A) and prevalence (Fig 2C) data from IP₃R$_{PS1WT}$ and IP₃R$_{PS1M146L}$ are given in Table 1. Notice that some of the parameters for IP₃R$_{PS1WT}$ are different from those in [22] because IP₃R$_{PS1WT}$ behaves somewhat differently from the IP₃R channel in wild type untransfected Sf9 cells (IP₃R$_{noPS1}$), despite the general similarity in the gating of the two (Fig 3A–3C, triangles for IP₃R$_{noPS1}$, squares and solid lines for IP₃R$_{PS1WT}$), especially P_o at $\mathcal{I} = 100nM$ and $400\ nM < \mathcal{C} \leq 1\mu M$. It is remarkable that the occupancy of only 4 states changes in the presence of PS1-M146L as compared to PS1-WT. The four states are $K_{O_{24}^H}$, $K_{O_{24}^I}$, $K_{O_{14}^I}$, and $K_{C_{32}^L}$
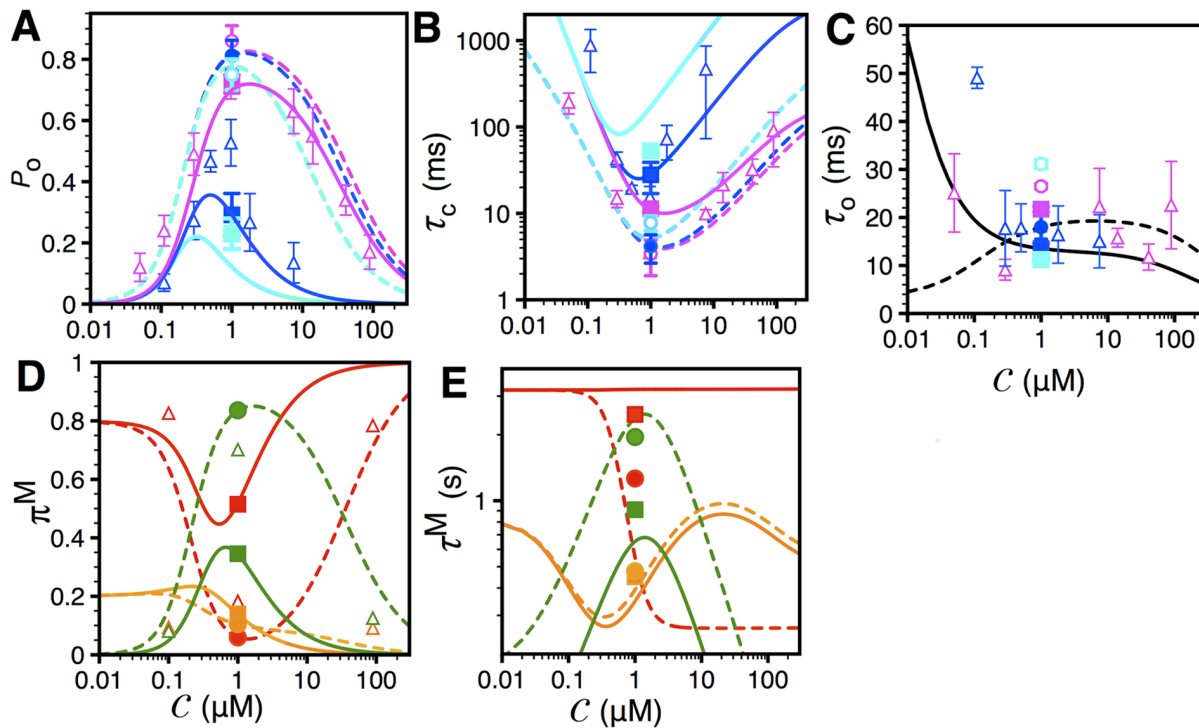
Fig 3. Mean gating properties of IP₃R in the presence of PS1-WT and PS1-M146L. Experimental values are shown by symbols (filled symbols for data that are used to derive the parameters for our model, open symbols for data not used for parameter derivation), theoretical values calculated from the twelve-state model using corresponding parameters are shown by lines. Mean P_o (A), τ_c (B), and τ_o (C) of IP₃R$_{PS1WT}$ (solid lines and squares) and IP₃R$_{PS1M146L}$ (dashed lines and circles) at $\mathcal{I}$ = 33nM, 100nM, and 10μM (in turquoise, blue, and magenta, respectively) as functions of $\mathcal{C}$. Data for $\mathcal{I}$ = 100nM (blue symbols) were published in [15], and data for $\mathcal{I}$ = 33 nM and 10 uM (turquoise and magenta symbols, respectively) were published in [14]. (C) Because experimental τ_o values did not show any strong systematic trend as $\mathcal{I}$ varied (from 33 nM through 100 nM to 10 μM), theoretical values of τ_o generated by the models for all $\mathcal{I}$ (33nM, 100 nM or 10 μM) are the same (shown in black, solid line for IP₃R$_{PS1WT}$ and dashed line for IP₃R$_{PS1M146L}$). Prevalences (D) and life-times (E) of the three gating modes (red, orange, and green for L, I, and H modes, respectively) of IP₃R$_{PS1WT}$ (solid lines and squares) and IP₃R$_{PS1M146L}$ (dashed lines and circles) as a function of $\mathcal{C}$ at $\mathcal{I}$ = 100nM. In (D), the open triangles are data for IP₃R$_{noPS1}$ at saturating $\mathcal{I}$ = 10μM [21] showing that modal prevalences of IP₃R$_{PS1M146L}$ at $\mathcal{I}$ = 100 nM are similar to those of IP₃R$_{noPS1}$ at $\mathcal{I}$ = 10μM. Error bars represent standard error of the mean.

doi:10.1371/journal.pcbi.1004529.g003

Table 1. Parameters for occupancies of all states in the model. Parameters for IP₃R$_{PS1M146L}$ are shown in bold if they are different from those for IP₃R$_{PS1WT}$. All other parameters are the same for IP₃R$_{PS1WT}$ and IP₃R$_{PS1M146L}$.

Parameters	Values
$K_{C^L_{00}}$	1
$K_{C^L_{20}}$	7.061 μM^{-2}
$K_{C^L_{30}}$	1.778 μM^{-3}
$K_{C^L_{32}}$	1.504 × 10^7 (**2.749 × 10^5**) μM^{-5}
$K_{C^L_{04}}$	1.746 × 10^8 μM^{-4}
$K_{C^I_{04}}$	4.365 × 10^7 μM^{-4}
$K_{C^H_{24}}$	3.082 × 10^8 μM^{-6}
$K_{C^I_{24}}$	3.0823 × 10^8 μM^{-4}
$K_{C^L_{34}}$	1.0319 × 10^8 μM^{-7}
$K_{O^I_{14}}$	6.605 × 10^7 (**8.478 × 10^7**) μM^{-5}
$K_{O^H_{24}}$	8.702 × 10^8 (**3.992 × 10^9**) μM^{-6}
$K_{O^I_{24}}$	5.856 × 10^7 (**1.006 × 10^8**) μM^{-6}

doi:10.1371/journal.pcbi.1004529.t001

Table 2. Transition rates between various states. In the following j_{ijmn} represents the flux parameter (see Table 3) and *rsr* stands for reciprocal of sum of reciprocals, i.e. $rsr(x, y) = 1/(1/x+1/y)$. For simplicity, we assume that the rates for the $C_{04}^I \to C_{24}^I$ & $C_{00}^L \to C_{20}^L$ transitions are equal to the rate for $C_{04}^I \to C_{24}^H$ transition while those for $C_{04}^I \leftarrow C_{24}^I$ & $C_{00}^L \leftarrow C_{20}^L$ transitions are equal to the rate for $C_{04}^I \leftarrow C_{24}^H$ transition.

Transition	Rates
$C_{04}^I \to C_{24}^H$	$rsr(j_{0414}\mathcal{C}, j_{1424}\mathcal{C}^2)/K_{C_{04}^I}$
$C_{04}^I \leftarrow C_{24}^H$	$rsr(j_{0414}\mathcal{C}, j_{1424}\mathcal{C}^2)/K_{C_{24}^H}\mathcal{C}^2$
$C_{24}^H \to O_{24}^H$	$j_{2424}^{HH}/K_{C_{24}^H}$
$C_{24}^H \leftarrow O_{24}^H$	$j_{2424}^{HH}/K_{O_{24}^H}$
$O_{24}^H \to C_{34}^L$	$j_{2434}\mathcal{C}/K_{O_{24}^H}$
$O_{24}^H \leftarrow C_{34}^L$	$j_{2434}/K_{C_{34}^L}$
$C_{04}^I \to C_{34}^L$	$rsr(j_{0414}^{IL}\mathcal{C}, j_{1424}^{IL}\mathcal{C}^2, j_{2434}^{IL}\mathcal{C}^3)/K_{C_{04}^I}$
$C_{04}^I \leftarrow C_{34}^L$	$rsr(j_{0414}^{IL}\mathcal{C}, j_{1424}^{IL}\mathcal{C}^2, j_{2434}^{IL}\mathcal{C}^3)/K_{C_{34}^L}\mathcal{C}^3$
$C_{04}^I \to O_{14}^I$	$j_{0414}^{II}\mathcal{C}/K_{C_{04}^I}$
$C_{04}^I \leftarrow O_{14}^I$	$j_{0414}^{II}/K_{O_{14}^I}$
$C_{24}^I \to O_{24}^I$	$j_{2424}^{II}/K_{C_{24}^I}$
$C_{24}^I \leftarrow O_{24}^I$	$j_{2424}^{II}/K_{O_{24}^I}$
$O_{24}^I \to O_{24}^H$	$j_{2424}/K_{O_{24}^I}$
$O_{24}^I \leftarrow O_{24}^H$	$j_{2424}/K_{O_{24}^H}$
$C_{04}^I \to C_{04}^L$	$j_{0404}/K_{C_{04}^I}$
$C_{04}^I \leftarrow C_{04}^L$	$j_{0404}/K_{C_{04}^L}$
$C_{32}^L \to C_{34}^L$	$j_{3334}\mathcal{I}^2/K_{C_{32}^L}$
$C_{32}^L \leftarrow C_{34}^L$	$j_{3334}/K_{C_{34}^L}$
$C_{30}^L \to C_{32}^L$	$j_{3132}\mathcal{I}^2/K_{C_{30}^L}$
$C_{30}^L \leftarrow C_{32}^L$	$j_{3132}/K_{C_{32}^L}$
$C_{20}^L \to C_{30}^L$	$j_{2030}\mathcal{C}/K_{C_{20}^L}$
$C_{20}^L \leftarrow C_{30}^L$	$j_{2030}/K_{C_{30}^L}$
$C_{00}^L \to C_{04}^I$	$rsr(j_{0001}\mathcal{I}, j_{0304}\mathcal{I}^4)$
$C_{00}^L \leftarrow C_{04}^I$	$rsr(j_{0001}, j_{0304}\mathcal{I}^3)/K_{C_{04}^I}\mathcal{I}^3$
$C_{20}^L \to C_{24}^H$	$rsr(j_{2021}\mathcal{I}, j_{2324}\mathcal{I}^4)$
$C_{20}^L \leftarrow C_{24}^H$	$rsr(j_{2021}, j_{2324}\mathcal{I}^3)/K_{C_{04}^L}\mathcal{I}^3$

doi:10.1371/journal.pcbi.1004529.t002

whose occupancies change by a factor of 4.587, 1.284, 1.718, and 0.018 respectively. Thus IP₃R$_{PS1M146L}$ spends relatively more time in the states $K_{O_{24}^H}$, $K_{O_{24}^I}$, and $K_{O_{14}^I}$ and less time in $K_{C_{32}^L}$ as compared to IP₃R$_{PS1WT}$. This is consistent with the prevalence data where there is a significant increase in π^H (0.345 vs 0.836) at the cost of π^L (0.515 vs 0.059) in IP₃R$_{PS1M146L}$ as compared to IP₃R$_{PS1WT}$. π^I on the other hand does not change significantly (0.14 vs 0.104) (Fig 2C). Thus the increase in P_o is mainly due to the significantly less time spent by IP₃R$_{PS1M146L}$ in C_{32}^L and more time spent in O_{24}^H (Fig 2B) as compared to IP₃R$_{PS1WT}$.

To derive the probability flux parameters used in the transition rates between different gating states (Table 2), we fit the model to idealized current traces recording openings and closings of IP₃R$_{PS1WT}$ and IP₃R$_{PS1M146L}$ by minimizing the likelihood score Eq (6) of the data. The flux parameters from the fits are given in Table 3. Only two of the eighteen flux parameters of

Table 3. Flux parameters used in the model. j_{ijmn} represent a flux parameter between a state with i Ca^{2+} ions and j IP$_3$ molecules and a state with m Ca^{2+} ions and n IP$_3$ molecules bound. Superscripts are used to distinguish between different flux parameters that connect different pairs of states that have the same numbers of ligands bound. For example, in both transitions $C_{24}^I \rightleftharpoons O_{24}^I$ and $C_{24}^H \rightleftharpoons O_{24}^H$, the channel is bound to the same number of Ca^{2+} and IP$_3$. However, the two transitions have different flux parameters because the channel is in different gating modes. The same font convention is used for the parameters as in Table 1.

Parameters	Pathway	Values	Units
j_{0414}	$C_{04}^I \rightleftharpoons C_{24}^H$	1.017×10^6	$\mu M^{-5}ms^{-1}$
j_{1424}	$C_{04}^I \rightleftharpoons C_{24}^H$	2.840×10^7	$\mu M^{-6}ms^{-1}$
j_{2434}	$O_{24}^H \rightleftharpoons C_{34}^L$	4.961×10^5	$\mu M^{-7}ms^{-1}$
j_{0414}^{IL}	$C_{04}^I \rightleftharpoons C_{34}^L$	9.502×10^8	$\mu M^{-5}ms^{-1}$
j_{1424}^{IL}	$C_{04}^I \rightleftharpoons C_{34}^L$	6.4×10^5	$\mu M^{-6}ms^{-1}$
j_{2434}^{IL}	$C_{04}^I \rightleftharpoons C_{34}^L$	2.431×10^3	$\mu M^{-7}ms^{-1}$
j_{2030}	$C_{20}^L \rightleftharpoons C_{30}^L$	2.449×10^{-3}	$\mu M^{-3}ms^{-1}$
j_{0414}^{II}	$C_{04}^I \rightleftharpoons O_{14}^I$	$5.156 \times 10^5 (\mathbf{2.587 \times 10^7})$	$\mu M^{-5}ms^{-1}$
j_{2424}^{II}	$C_{24}^I \rightleftharpoons O_{24}^I$	3.0577×10^7	$\mu M^{-7}ms^{-1}$
j_{2424}	$O_{24}^I \rightleftharpoons O_{24}^H$	3.301×10^5	$\mu M^{-6}ms^{-1}$
j_{0404}	$C_{04}^I \rightleftharpoons C_{04}^L$	5.459×10^4	$\mu M^{-4}ms^{-1}$
j_{2424}^{HH}	$C_{24}^H \rightleftharpoons O_{24}^H$	$5.478 \times 10^7 (\mathbf{1.753 \times 10^8})$	$\mu M^{-6}ms^{-1}$
j_{3132}	$C_{30}^L \rightleftharpoons C_{34}^L$	2.891×10^{-2}	$\mu M^{-5}ms^{-1}$
j_{3334}	$C_{32}^L \rightleftharpoons C_{34}^L$	2.120×10^3	$\mu M^{-7}ms^{-1}$
j_{0001}	$C_{00}^L \rightleftharpoons C_{04}^I$	1.138×10^{-2}	$\mu M^{-1}ms^{-1}$
j_{0304}	$C_{00}^L \rightleftharpoons C_{04}^I$	4.756×10^{10}	$\mu M^{-4}ms^{-1}$
j_{2021}	$C_{20}^L \rightleftharpoons C_{24}^H$	8.904×10^{-4}	$\mu M^{-3}ms^{-1}$
j_{2324}	$C_{20}^L \rightleftharpoons C_{24}^H$	8.523×10^6	$\mu M^{-6}ms^{-1}$

doi:10.1371/journal.pcbi.1004529.t003

IP$_3$R$_{PS1M146L}$ are different from IP$_3$R$_{PS1WT}$ (shown in bold). These two parameters are involved in the $C_{04}^I \leftrightarrow O_{14}^I$ and $C_{24}^H \leftrightarrow O_{24}^H$ transitions and are higher for IP$_3$R$_{PS1M146L}$ as compared to IP$_3$R$_{PS1WT}$.

The mean gating properties of the channel as a function of $\mathcal{C}$ at different $\mathcal{I}$ values are shown in Fig 3. Theoretical values of the P_o of IP$_3$R$_{PS1WT}$ (Fig 3A, solid lines) and IP$_3$R$_{PS1M146L}$ (Fig 3A, dashed lines) were generated by using Eq (2) and the occupancy parameters in Table 1. The P_o of IP$_3$R$_{PS1M146L}$ at $\mathcal{I} = 33$nM (turquoise dashed line and turquoise circle) and 100nM (blue dashed line and blue circle) are significantly larger than P_o of IP$_3$R$_{PS1WT}$ at $\mathcal{I} = $ 100nM (solid blue line and blue square). In fact, the P_o of IP$_3$R$_{PS1M146L}$ at $\mathcal{I} = 33$nM is comparable to P_o of IP$_3$R$_{PS1WT}$ (magenta square and solid line) or IP$_3$R$_{noPS1}$ (magenta triangles from [23]) at saturating $\mathcal{I} = 10\mu$M. The P_o data for IP$_3$R$_{noPS1}$ at saturating $\mathcal{I} = 10\mu$M is shown for comparison to emphasize that IP$_3$R$_{PS1M146L}$ is already maximally activated at a significantly lower $\mathcal{I}$ of 100nM. This clearly indicates that IP$_3$R in the presence of FAD-causing mutant PS is highly sensitized to activation by IP$_3$, and is maximally activated at significantly lower $\mathcal{I}$ than IP$_3$R$_{PS1WT}$ or IP$_3$R$_{noPS1}$. For $\mathcal{C} > 800$nM, P_o of IP$_3$R$_{PS1M146L}$ at $\mathcal{I} = 10\mu$M (magenta dashed line and magenta circle) is higher than that of IP$_3$R$_{noPS1}$ or IP$_3$R$_{PS1WT}$ at the corresponding $\mathcal{I}$ and $\mathcal{C}$, mostly due to the higher saturating P_o of IP$_3$R$_{PS1M146L}$ (0.86 ± 0.03) as compared to those of IP$_3$R$_{noPS1}$ (0.72 ± 0.03) [23] and IP$_3$R$_{PS1WT}$ (0.72 ± 0.05) [15]. A close examination of τ_c (Fig 3B) and τ_o (Fig 3C) reveals that the increase in P_o of IP$_3$R$_{PS1M146L}$ is mostly due to the substantial shortening of τ_c with relatively modest increase in τ_o. Theoretical values of τ_o and τ_c were

calculated using Eq (7) and the parameters in Tables 1 and 3. Gating properties (P_o, τ_o, and τ_c) of IP$_3$R$_{noPS1}$ in $\mathcal{I}$ = 100nM and 10μM observed in [23] (triangles in Fig 3A–3C) are similar to theoretical values calculated for IP$_3$R$_{PS1WT}$, since IP$_3$R$_{PS1WT}$ gating is generally similar to that of IP$_3$R$_{noPS1}$, as observed in [14], albeit with some noticeable differences (Fig 3A–3C). The open triangles in Fig 3A–3C representing data from [23] of IP$_3$R$_{noPS1}$ in wild type Sf9 cells is shown here to demonstrate that the model for IP$_3$R$_{PS1WT}$ can replicate reasonably well the P_o, τ_o, and τ_c of IP$_3$R channel gating in the absence of PS1.

Next, we calculated with our modified data-driven model the prevalence of the three gating modes using Eq (3) and occupancy parameters given in Table 1 (Fig 3D and 3E). Both experimental (symbols) and theoretical (lines) results show a significant increase in π^H (green), and decrease in π^L (red) for IP$_3$R$_{PS1M146L}$ (dashed lines and circles) as compared to IP$_3$R$_{PS1WT}$ (solid lines and squares) (Fig 3D) at $\mathcal{C}$ = 1μM and $\mathcal{I}$ = 100 nM. π^I (orange), on the other hand, remains largely unchanged. Comparison with the prevalence data from IP$_3$R in untransfected Sf9 cells at saturating $\mathcal{I}$ = 10μM (triangles) from [21] confirms the saturating activation of IP$_3$R$_{PS1M146L}$ at relatively low $\mathcal{I}$. The mean life-times of the three gating modes follow a similar trend as seen in their prevalences. τ^H is longer, τ^L is shorter, while τ^I remains unchanged for IP$_3$R$_{PS1M146L}$ as compared to IP$_3$R$_{PS1WT}$ (Fig 3E). The theoretical modal mean life-times were calculated from our modified model by using Eq (9) and parameters in Tables 1 and 3.

The open and closed dwell-time distributions were calculated from the model as described in the Dwell-Time Distributions section Eqs (14) and (15) using occupancy and flux parameters in Tables 1 and 3 respectively. As shown in Fig 4, the model (red lines) fits the observed dwell-time distributions (gray bars) very well. Consistent with the τ_o observed (Fig 3C), there is a minor right-shift in the open dwell-time distribution of IP$_3$R$_{PS1M146L}$ (Fig 4C) as compared to IP$_3$R$_{PS1WT}$ (Fig 4A). Thus, PS1-M146L does not have significant effect on τ_o of the IP$_3$R channel. The close dwell-time distribution of IP$_3$R$_{PS1M146L}$ (Fig 4D), on the other hand, shows significant shift to the left when compared to IP$_3$R$_{PS1WT}$ (Fig 4B), leading to the shorter τ_c and therefore the higher P_o observed.

The Dwell-Time Distributions section also describes the derivation of the open and closed dwell-time distributions in H and I modes from the model. The dwell-time distributions from the model for $\mathcal{C}$ = 1μM and $\mathcal{I}$ = 100nM in the H (Fig 5A–5D) and I (Fig 5E–5H) modes calculated by using Eqs (18) and (19) and parameters in Tables 1 and 3 are given by red lines. The experimental data are presented by the gray bars for comparison. A close inspection of the modal open and closed dwell-time distributions of IP$_3$R$_{PS1WT}$ and IP$_3$R$_{PS1M146L}$ provides useful insight into the modal behavior of the channel. In line with the over-all open dwell-time distribution, the open dwell-time distributions in the H (Fig 5A, 5C) and I (Fig 5E, 5F) modes do not change significantly. The closed dwell-time distributions in the two modes in IP$_3$R$_{PS1M146L}$ (Fig 5D, 5H) on the other hand, shift significantly to the left as compared to IP$_3$R$_{PS1WT}$ (Fig 5B, 5G). Furthermore, the shift in the closed dwell-time distribution in the H mode is more significant (Fig 5B, 5D). This suggests that the relatively shorter time spent by IP$_3$R$_{PS1M146L}$ in the H mode's closed state plays a major role in the shortening of τ_c and hence enhancement of P_o of the channel in the presence of FAD-causing mutation as compared to wild-type PS1.

To gain further insights and quantify the extent of IP$_3$R sensitization due to PS1-M146L, we extrapolate the P_o, τ_c, and the mean modal properties of IP$_3$R at different values of $\mathcal{C}$ and $\mathcal{I}$ from our model using parameters tabulated in Tables 1 and 3. Fig 6A shows P_o of IP$_3$R$_{PS1WT}$ (black solid lines) and IP$_3$R$_{PS1M146L}$ (blue dashed lines) as a function of $\mathcal{C}$ at different $\mathcal{I}$, calculated using Eq (2). Even at $\mathcal{I}$ = 8nM, P_o of IP$_3$R$_{PS1M146L}$ is already higher than that of IP$_3$R$_{PS1WT}$ at $\mathcal{I}$ = 100nM (thick solid black line) for all $\mathcal{C}$. Thus, whereas IP$_3$R$_{PS1WT}$ in 8 nM IP$_3$ are minimally active ($P_o \sim 0.005$) in resting $\mathcal{C}$ ($\sim$ 70 nM), IP$_3$R$_{PS1M146L}$ under the same ligand conditions can have sufficient activity ($P_o > 0.04$) to initiate intracellular Ca^{2+} signals.
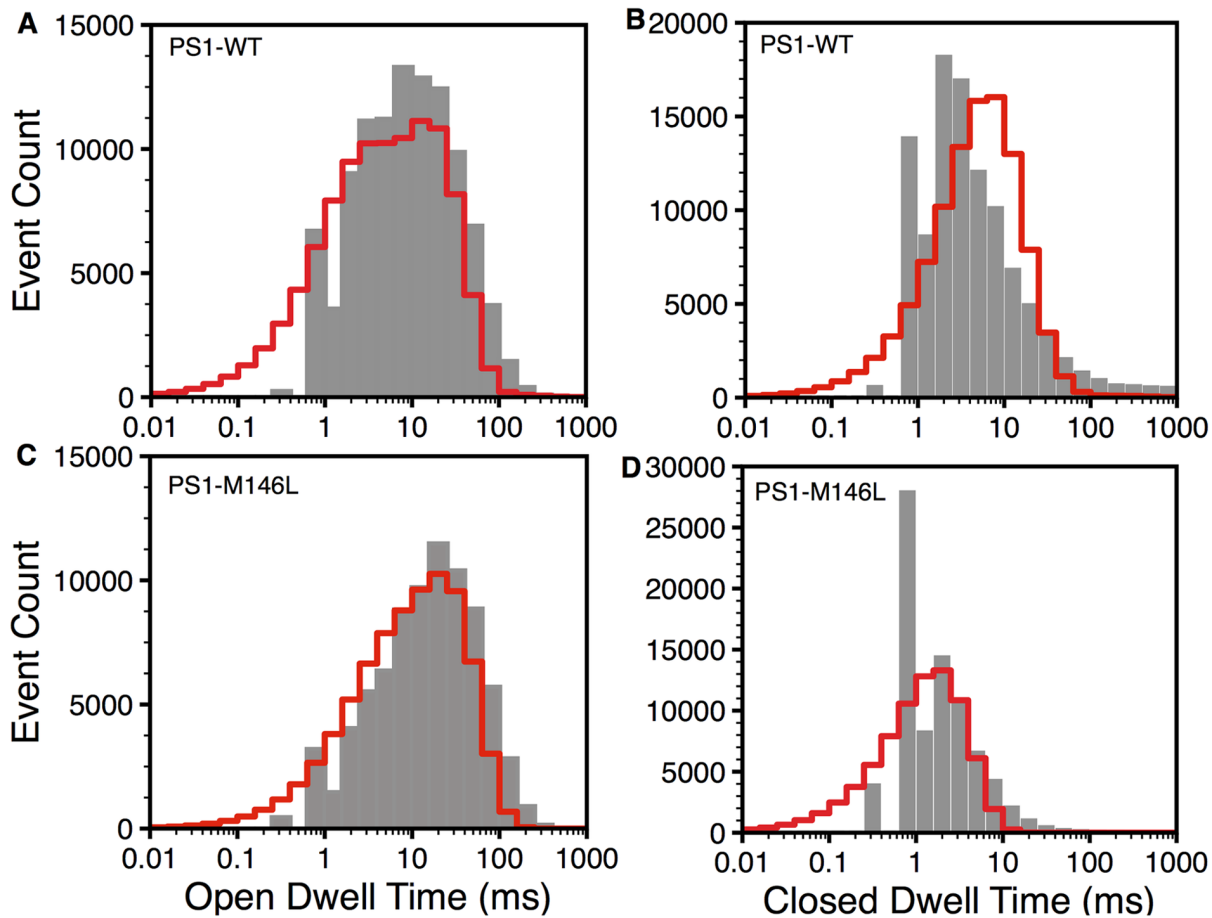
Fig 4. Dwell time distributions of IP$_3$R. Open (A) and closed (B) dwell time distributions of IP$_3$R in the presence of PS1-WT and open (C) and closed (D) dwell time distributions of IP$_3$R in the presence of PS1-M146L at $\mathcal{C}$ = 1μM and $\mathcal{I}$ = 100nM. Bars and lines respectively represent experimental data and model.
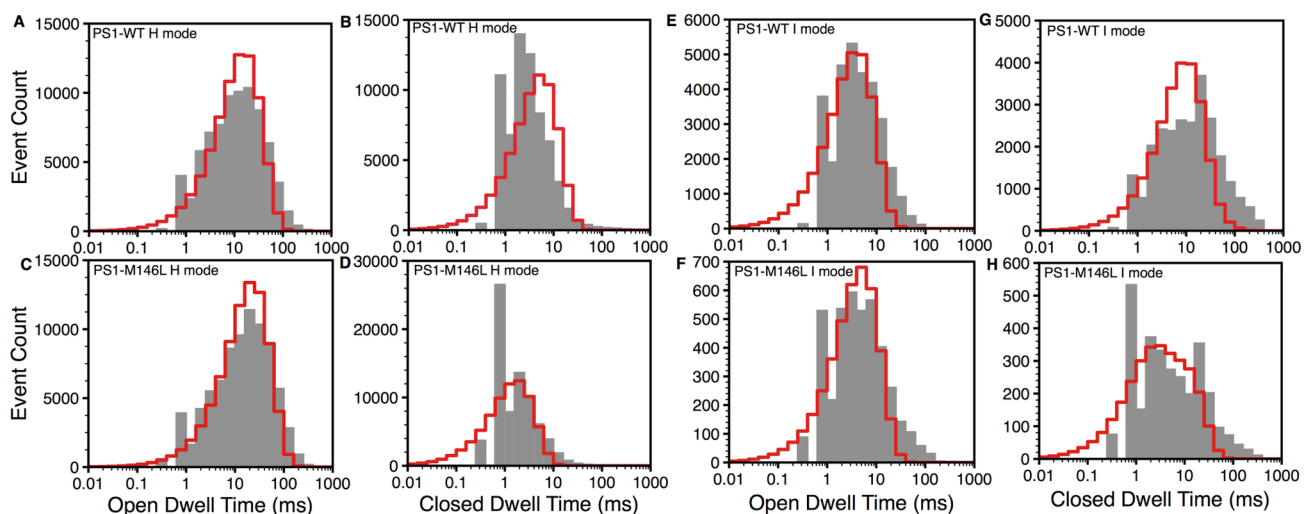
doi:10.1371/journal.pcbi.1004529.g004

Fig 5. Dwell-time distributions in H and I modes at at $\mathcal{C}$ = 1μM and $\mathcal{I}$ = 100nM. Top and bottom rows are for IP$_3$R$_{PS1WT}$ and IP$_3$R$_{PS1M146L}$ respectively. Open (A, C) and closed (B, D) dwell-time distributions in H mode. Open (E, F) and closed (G, H) dwell-time distributions in I mode. Bars are the experimental values and lines are the model fits.

doi:10.1371/journal.pcbi.1004529.g005
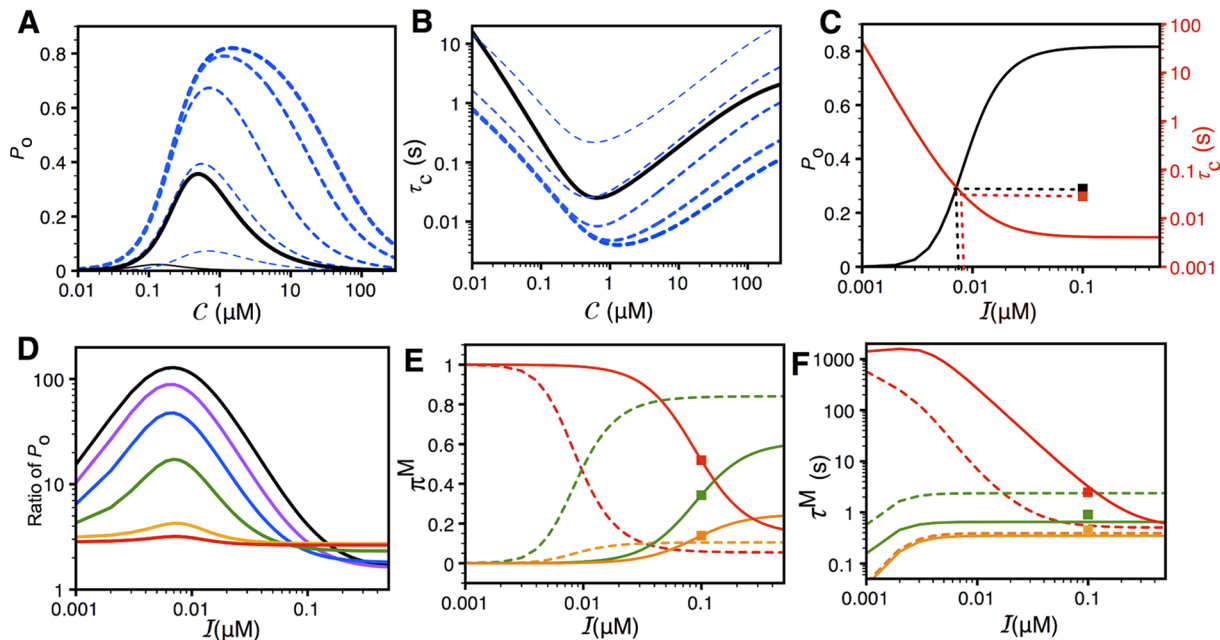
Fig 6. Quantifying the sensitization of IP₃R in the presence of FAD mutant through simulations. The lines are from the model while the squares in panels (C, E, and F) are the experimental values for IP₃R$_{PS1WT}$ at $\mathcal{C} = 1\mu M$ and $\mathcal{I} = 100nM$. The increasing thicknesses of the lines in (A) and (B) represent increasing IP₃ concentration. (A) P_o of IP₃R$_{PS1WT}$ at $\mathcal{I} = 8nM$ and $100nM$ (black solid lines) and IP₃R$_{PS1M146L}$ at $\mathcal{I} = 4nM$, $8nM$, $16nM$, $40nM$, and $100nM$ (blue dashed lines) as a function of $\mathcal{C}$. (B) The τ_c of the channel from simulations in (A) where the thicknesses, colors, and styles of the lines have the same meanings as in (A), τ_c of IP₃R$_{PS1WT}$ at $\mathcal{I} = 8nM$ is not shown. (C) The P_o (black) and τ_c (red) of IP₃R$_{PS1M146L}$ as a function of $\mathcal{I}$ at $\mathcal{C} = 1\mu M$. The vertical and horizontal black and red dotted lines respectively represent the $\mathcal{I}$ value ($\sim 8nM$) at which the P_o and τ_c of IP₃R$_{PS1M146L}$ cross the P_o and τ_c of IP₃R$_{PS1WT}$ at $\mathcal{C}$ $= 1\mu M$ and $\mathcal{I} = 100nM$. (D) The ratio of the P_o of IP₃R$_{PS1M146L}$ to that of IP₃R$_{PS1WT}$ as a function of $\mathcal{I}$ at $\mathcal{C} = 70nM$ (red), $100nM$ (yellow), $250nM$ (green), $500nM$ (blue), $1\mu M$ (purple), and $2\mu M$ (black). (E) and (F) show the prevalences and mean life-times respectively of L (red), I (orange), and H (green) modes of IP₃R$_{PS1WT}$ (solid lines) and IP₃R$_{PS1M146L}$ (dashed lines) as a function of $\mathcal{I}$ at $\mathcal{C} = 1\mu M$. Squares represent values observed in [15].

doi:10.1371/journal.pcbi.1004529.g006

The τ_c of the channels from simulation Eq (7) in Fig 6B correlate well with the P_o values (notice that at fixed $\mathcal{I}$, P_o decreases as τ_c increases and vice versa). This close correlation between the P_o and τ_c is the consequence of the lack of dependence of the τ_o on $\mathcal{I}$ (see Eq (7) and Fig 3C). Thus for $\mathcal{I} > 8$ nM, τ_c of IP₃R$_{PS1M146L}$ (blue dashed lines) is shorter than that of IP₃R$_{PS1WT}$ at $\mathcal{I} = 100nM$ (black solid line) for all physiological $\mathcal{C}$ values. Whereas the strong Ca²⁺ activation of IP₃R$_{PS1M146L}$ between $\mathcal{C} = 0.01$ and 0.5 μM remains the same as $\mathcal{I}$ is raised from 16 to 100 nM, channel P_o for higher $\mathcal{C}$ does increase as $\mathcal{I}$ increases from 16 nM to 1 μM, confirming the higher saturating P_o of IP₃R$_{PS1M146L}$ as described above (Fig 3A) and is in line with observations (Table S1 in [14]).

To quantitatively compare the sensitivity of IP₃R$_{PS1WT}$ and IP₃R$_{PS1M146L}$ to activation by IP3, we plot in Fig 6C the P_o of IP₃R$_{PS1M146L}$ as a function of $\mathcal{I}$ at fixed $\mathcal{C} = 1\mu M$ (black line) and the experimentally observed P_o of IP₃R$_{PS1WT}$ at $\mathcal{C} = 1\mu M$ and $\mathcal{I} = 100$ nM (black square). The plot reveals that P_o of IP₃R$_{PS1M146L}$ at $\mathcal{I} = 8$ nM already exceeds that of IP₃R$_{PS1WT}$ at $\mathcal{I} = 100$ nM (see black dotted lines). In contrast, P_o of IP₃R$_{PS1WT}$ is negligible at $\mathcal{I} = 8nM$ and $\mathcal{C} = 1\mu M$ (Fig 6A, black thin solid line). Correspondingly, τ_c of IP₃R$_{PS1M146L}$ (red line in Fig 6C) becomes shorter than the observed τ_c of IP₃R$_{PS1WT}$ (red square) at $\mathcal{I} = 100nM$ as $\mathcal{I}$ is raised beyond 8nM.

In Fig 6D, we show the ratio of simulated P_o of IP₃R$_{PS1M146L}$ to that of IP₃R$_{PS1WT}$ as a function of $\mathcal{I}$ at $\mathcal{C} = 70nM$, $100nM$, $250nM$, $500nM$, $1\mu M$, and $2\mu M$. For $\mathcal{I} < 200nM$, IP₃R$_{PS1M146L}$ is more than twice as active as IP₃R$_{PS1WT}$ for all $\mathcal{I}$ and $\mathcal{C}$ values. For physiological resting $\mathcal{C} =$

70nM, IP$_3$R channel activity is enhanced by 265% in cells expressing PS1-M146L relative to that in PS1-WT expressing cells. For optimal $\mathcal{C}$, IP$_3$R$_{PS1M146L}$ exhibits a gain-of-function enhancement by over 100 folds as compared to IP$_3$R$_{PS1WT}$, with maximum enhancement occurring around $\mathcal{I}$ = 7–8 nM IP$_3$. The drop in the P_o ratio for $\mathcal{I} > 8$nM is due to the fact that P_o of IP$_3$R$_{PS1M146L}$ peaks much faster than IP$_3$R$_{PS1WT}$ as a function of $\mathcal{I}$.

At fixed $\mathcal{C}$ = 1μM, the theoretical π^L Eq (3) of IP$_3$R$_{PS1M146L}$ decreases for 2nM $< \mathcal{I} <$ 100nM and plateaus outside this window (Fig 6E, dashed red line). π^H of IP$_3$R$_{PS1M146L}$ (dashed green line) changes in the opposite direction for 2nM $< \mathcal{I} <$ 100nM. π^I of IP$_3$R$_{PS1M146L}$ (dashed orange line), on the other hand, remains largely constant. Around $\mathcal{I}$ = 8 nM, both the π^L and π^H curves of IP$_3$R$_{PS1M146L}$ crosses the observed π^L (red square) and π^H (green square) levels, respectively, of IP$_3$R$_{PS1WT}$ measured at $\mathcal{I}$ = 100nM and $\mathcal{C}$ = 1μM. π^I of IP$_3$R$_{PS1M146L}$ gets close to but does not exceed that of IP$_3$R$_{PS1WT}$ observed at $\mathcal{I}$ = 100nM and $\mathcal{C}$ = 1μM (orange square). This indicates that the increase in P_o of IP$_3$R in the presence of PS1-M146L is mainly due the switching of the channel from L to H mode. Interestingly, the $\mathcal{I}$ value ($\sim$ 10nM) where π^L and π^H cross each other is almost the same as where P_o reaches half (0.41) of its peak value (0.82) (see black line in Fig 6C). This is in line with the observations that mode switching is the major mechanism of ligand regulation of IP$_3$R [21]. Our results confirm that the mechanism of ligand regulation of IP$_3$R is mainly due to the switching of the channel between L and H modes with minimal contributions from I mode [21]. Furthermore, switching of IP$_3$R$_{PS1M146L}$ from L to H mode in comparison to IP$_3$R$_{PS1WT}$ translates into the gain-of-function enhancement of IP$_3$R gating. Fig 6E also shows how theoretical values of the prevalences of the three gating modes for IP$_3$R$_{PS1WT}$ vary with $\mathcal{I}$ at $\mathcal{C}$ = 1μM (solid lines).

Theoretical values of the mean life-times of I (orange) and H (green) mode calculated using Eq (9) at $\mathcal{C}$ = 1μM remain largely unchanged for all values of $\mathcal{I} > 3$nM (Fig 6F). In that range of $\mathcal{I}$, τ^H of IP$_3$R$_{PS1M146L}$ (dashed green line) is shorter than τ^H of IP$_3$R$_{PS1WT}$ (solid green line), while τ^I of IP$_3$R$_{PS1M146L}$ (dashed orange line) remains almost the same as τ^I of IP$_3$R$_{PS1WT}$ (solid orange line). For $\mathcal{I} < 4$nM, τ^I of IP$_3$R$_{PS1M146L}$ drops below the observed value for IP$_3$R$_{PS1WT}$ at $\mathcal{I}$ = 100nM. Simulated τ^L of IP$_3$R$_{PS1M146L}$ (dashed red line), on the other hand, decreases significantly as $\mathcal{I}$ increases. As $\mathcal{I}$ increases beyond 15 nM, simulated τ^L of IP$_3$R$_{PS1M146L}$ becomes shorter than that of IP$_3$R$_{PS1WT}$ measured at $\mathcal{I}$ = 100nM (red square). Relatively speaking, this does not correlate very closely with the $\mathcal{I}$ = 8nM where the P_o of IP$_3$R$_{PS1M146L}$ crosses the observed P_o of IP$_3$R$_{PS1WT}$ (Fig 6A) when compared to the prevalences where this critical value of $\mathcal{I}$ is 8nM. Nevertheless, the shorter τ^L will increase the P_o of IP$_3$R$_{PS1M146L}$. Thus the shorter τ^L and longer τ^H contribute to its increased sensitivity to IP$_3$ as compared to IP$_3$R$_{PS1WT}$.

To investigate how the remodeling of single IP$_3$R channel gating kinetics in the presence of mutant PS1-M146L affects the dynamics of IP$_3$R-mediated Ca^{2+} release events, we simulated such events at a Ca^{2+}-release site consisting of a cluster of ten IP$_3$Rs as described in the Methods Section. 400 s-long records of Ca^{2+} blips and puffs (Ca^{2+}-release events involving just one, or multiple IP$_3$R channels in the cluster, respectively) from the IP$_3$R cluster were generated, and statistics about these Ca^{2+}-release events were derived as described previously [28]. In line with observations reported in [35, 12], the site produces significantly potentiated puffs in the presence of FAD-causing PS1. As shown in Fig 7, the behavior of puffs and blips arising from a cluster of IP$_3$R$_{PS1M146L}$ (dashed lines with circles) is significantly different from that of a IP$_3$R$_{PS1WT}$ cluster (solid line with squares). Puffs from a IP$_3$R$_{PS1M146L}$ cluster have significantly larger amplitudes (Fig 7A), longer life times (Fig 7B), and take longer to terminate (Fig 7C). Furthermore, puff frequency in cells expressing PS1-M146L is significantly higher than that in PS1-WT-expressing cells (10.33/sec versus 1.83/sec) (Fig 7D). Interestingly, the statistics of Ca^{2+} blips are very similar in both case. Although the life times of blips in PS1-M146L-expressing cells is slightly longer than that in PS1-WT-expressing cells (Fig 7E), frequencies of the
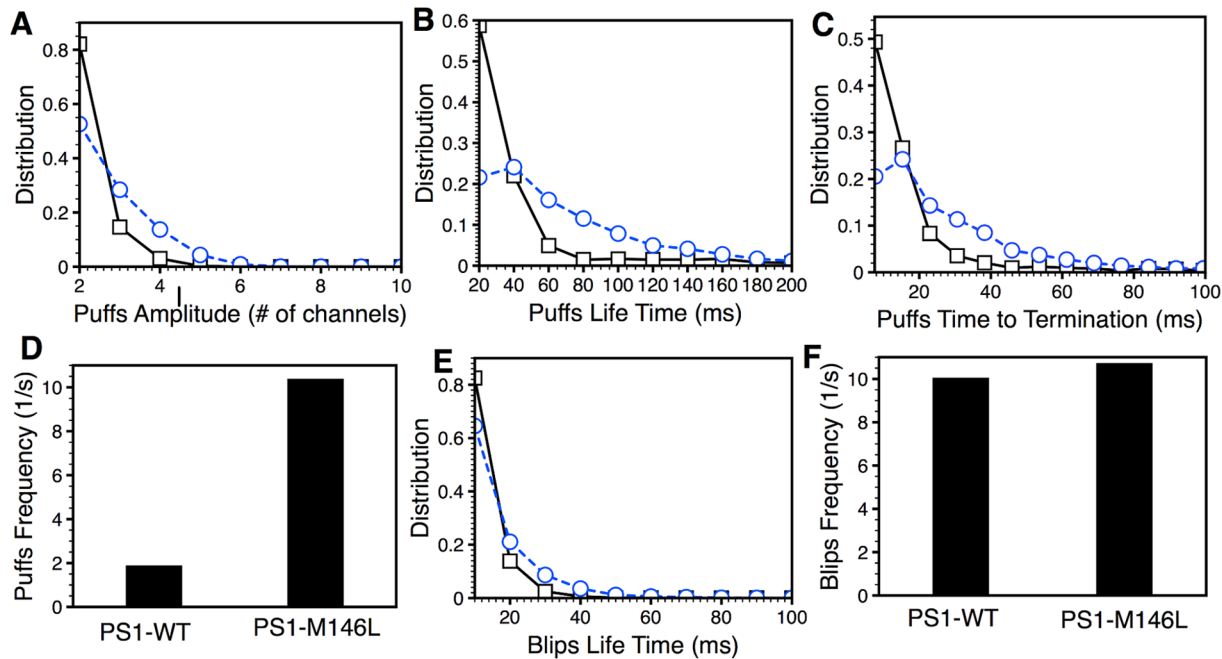
Fig 7. The statistics of Ca²⁺ puffs and blips change significantly in the presence of PS1-M146L (dashed lines with circles) as compared to PS1-WT (solid lines with squares). (A) Distribution of puff peak amplitude, (B) life time (duration from the start of the puff to the end of the puff), and (C) termination time (duration from the time at which maximum number of channels are open to the time when the last active channel becomes inactive). (D) Life time distribution of blips. Frequency of puffs (E) and blips (F). Simulations were performed at 100nM IP₃ concentration.

doi:10.1371/journal.pcbi.1004529.g007

blips are almost the same (10.67/sec versus 9.99/sec) ([Fig 7F](#)). Thus the higher number of single-channel events caused by higher sensitivity of $IP_3R_{PS1M146L}$ to activation by IP_3 translates into triggering more frequent and longer puffs.

Discussion

Accumulation of $A\beta$ aggregates and intracellular neurofibrillary tangles of τ protein are the main symptoms of AD [1]. However, most drugs focused on restricting $A\beta$ production and accumulation or enhancing its clearance from the brain have yielded disappointing results [36]. This could be due to the fact that these drugs target the late stage features of the disease, i.e. plaque formation—whereas there is poor correlation between $A\beta$ deposits and the progressive memory loss and cognitive decline observed [37]. Compelling evidence suggests that FAD-causing mutant PS disrupt intracellular Ca²⁺ signaling before $A\beta$ deposition, pointing towards the up-regulated Ca²⁺ signaling as a proximal event that could be involved in disease pathogenesis. Previously, we showed that FAD-causing mutant PS interact with ER-localized IP₃Rs, leading to their gain-of-function enhanced channel activity [14, 15]. However, further analysis is needed to elucidate the modified gating properties leading to the gain-of-function enhancement of IP₃R channel activity and to quantify their sensitization due to FAD-causing PS mutations.

Our modeling results show that there is a significant increase in the H mode prevalence, and a corresponding significant reduction in the L mode prevalence of IP₃R channels in the presence of PS1-M146L. This change in the prevalence of L and H modes arises mainly from the shorter mean life-time of the L mode and longer mean-life-time of the H mode. On the

other hand, both the life-time and prevalence of I mode remain constant. Our model predicts that the P_o of IP$_3$R$_{PS1M146L}$ saturates at significantly lower IP$_3$ concentrations and its peak value is higher compared to that of IP$_3$R$_{PS1WT}$. Furthermore, our model predicts that the channel's gain-of-function enhancement is sensitive to both IP$_3$ and Ca^{2+} ([Fig 6A](#)). Interestingly, our model predicts that the higher P_o of IP$_3$R$_{PS1M146L}$ as compared to IP$_3$R$_{PS1WT}$ is mainly due to the lower occupancy of C$_{32}^L$ state and higher occupancy of the O$_{24}^H$ state (with small change in the occupancies of O$_{24}^I$ and O$_{14}^I$). This means that PS1-M146L interacts with IP$_3$R in such a way that the closed configuration of the channel with 3 Ca^{2+} ions and 2 IP$_3$ bound is less likely and the open configuration in the H mode with 2 Ca^{2+} ions and 4 IP$_3$ molecules bound more easily attainable. The changes in the occupancies of states O$_{24}^H$ and C$_{32}^L$ lead to the increase in the prevalence of H mode and the corresponding decrease in the prevalence of L mode, resulting in the gain-of-function enhancement of IP$_3$R gating in the presence of PS1-M146L.

Our goal in this study was to use all the data at our disposal to model the gating kinetics of IP$_3$R$_{PS1WT}$ and IP$_3$R$_{PS1M146L}$; and use resulting models to simulate the behavior of IP$_3$R$_{PS1WT}$ and IP$_3$R$_{PS1M146L}$ in a wide range of ligand concentrations to gain a better understanding of how the gain-of-function enhancement of IP$_3$R$_{PS1M146L}$ alters the characteristics of local Ca^{2+} release events at IP$_3$R clusters.

Because of the considerable technical difficulties in obtaining single-channel current records of IP$_3$R channels in their native membrane milieu by nuclear patch clamp electrophysiology, the most comprehensive set of such single-channel data (including steady-state gating records over a broad range of combinations of cytoplasmic IP$_3$ and Ca^{2+} [23], long gating records in multiple constant ligand conditions suitable for modal gating analysis [21], records of response kinetics of IP$_3$R channel to rapid changes in cytoplasmic ligand conditions [38]) was obtained in the study of the endogenous IP$_3$R from insect Sf9 cells. This set of data was used to develop the twelve-state kinetic model [22] that provides the basis of the models we develop here to simulate the behavior of the endogenous Sf9 IP$_3$R in the presence of exogenous recombinant human PS1 (WT and mutant). Until a comparable or more comprehensive set of single-channel data for a mammalian IP$_3$R becomes available, our approach is the best that can be achieved to simulate gating behaviors of IP$_3$R interacting with WT and mutant PS1. Although Sf9 IP$_3$R does not interact with human PS1 in its natural environment, the study in [15] showed that endogenous IP$_3$R in human lymphoblasts in presence of PS1-M146L exhibits very similar changes in its gating characteristics (increase in P_o and τ_o with corresponding reduction in τ_c) and modal gating behavior (rise in π^H with simultaneous drop in π^L) when compared to IP$_3$R in the presence of PS1-WT. Therefore, we have reason to be confident that simulation results from our modeling effort do reflect the gating behaviors of IP$_3$R naturally interacting with WT and mutant PS1, and that the insights our effort provides about the effects of mutant PS1 on IP$_3$R single-channel gating and local intracellular Ca^{2+} release events can improve our understanding of the pathophysiology of FAD.

The higher prevalence and longer life-time of H mode and shorter life-time of L mode for IP$_3$R$_{PS1M146L}$ may have important implications for cell physiology. Since the open time in the H mode is significantly higher than that in the L mode, in which the channel has near-zero mean open time, IP$_3$R gating in the H mode will have higher probability of activating neighboring channels through Ca^{2+}-induced-Ca^{2+} release (CICR), thus leading to higher frequency of Ca^{2+} puffs ([Fig 7D](#)). The higher sensitivity of IP$_3$R$_{PS1M146L}$ to activation by Ca^{2+} and IP$_3$ also increases the number of open channels in an IP$_3$R channel cluster during a puff, leading to bigger ([Fig 7A](#)) and longer ([Fig 7B](#)) puffs, which in turn will cause more frequent global Ca^{2+} waves and oscillations at the cellular level, in line with observations [35, 12]. The higher prevalence of IP$_3$R channel being in the H mode resulting in the higher probability of inducing

global Ca^{2+} events can account for the higher frequency of Ca^{2+} oscillations in B lymphoblasts from FAD patients and DT40 cells expressing FAD-causing mutant PS [14, 15].

Our model reveals that even at resting level of $\mathcal{I}$ (8 nM), $IP_3R_{PS1M146L}$ exhibits significant P_o of 0.35 (40% of the P_o when the channel is in saturating $\mathcal{I}$) at $\mathcal{C} = 1\mu M$ whereas the P_o of IP_3R_{PS1WT} in the same ligand condition is negligible. This will lead to stronger CICR among channels in the same cluster and between IP_3R channel clusters, thereby generating more global spontaneous Ca^{2+} oscillations in cells expressing FAD-causing mutant PS as observed experimentally [14, 15].

To conclude, our study provides insights into the gating modulation of IP_3R that leads to the gain-of-function enhancement due to FAD-causing mutations in PS. Furthermore, significant activity exhibited by IP_3R at resting IP_3 concentration in cells expressing FAD-causing mutant can explain the spontaneous global Ca^{2+} signals observed in those cells. The models developed here for single-channel IP_3R channel gating and local Ca^{2+}-release events can provide part of the foundation for building whole-cell models to judiciously separate the key pathways leading to the global Ca^{2+} signaling dysregulation in AD from those that are by-products due to the CICR nature of Ca^{2+} signaling. For example, what are the relative contributions of gain-of-function enhancement and over-expression of ryanodine receptors [39, 20] to Ca^{2+} signaling dysregulation in AD? Does the down-regulation of Ca^{2+} buffers such as calbindin [40, 41] and higher resting Ca^{2+} concentration [42] play a role (through CICR mechanism) in the exaggerated Ca^{2+} signals? What are the conditions or factors that would reverse the exaggerated Ca^{2+} signaling back to normal state? These and many other interesting questions are the focus of our future research and the models developed here will play a key role in addressing them.

Supporting Information

S1 Text. Stochastic scheme and diffusion of Ca^{2+} and dye buffer.
(PDF)

Author Contributions

Conceived and designed the experiments: DODM KHC JKF GU. Performed the experiments: DODM KHC PT GU. Analyzed the data: DODM KHC PT GU. Contributed reagents/materials/analysis tools: DODM KHC PT JKF GU. Wrote the paper: DODM KHC PT GU.

References

1. Mattson MP (2004) Pathways towards and away from Alzheimer's disease. Nature 430: 631–639. doi: 10.1038/nature02621 PMID: 15295589

2. Hardy J, Selkoe DJ (2002) The amyloid hypothesis of Alzheimer's disease: progress and problems on the road to therapeutics. Science 297: 353–356. doi: 10.1126/science.1072994 PMID: 12130773

3. LaFerla FM (2002) Calcium dyshomeostasis and intracellular signalling in Alzheimer's disease. Nature Reviews Neuroscience 3: 862–872. doi: 10.1038/nrn960 PMID: 12415294

4. Xia W, Zhang J, Kholodenko D, Citron M, Podlisny MB, et al. (1997) Enhanced production and oligomerization of the 42-residue amyloid β-protein by chinese hamster ovary cells stably expressing mutant presenilins. Journal of Biological Chemistry 272: 7977–7982. doi: 10.1074/jbc.272.12.7977 PMID: 9065468

5. Hutton M (1997) The presenilins and Alzheimer's disease. Human molecular genetics 6: 1639–1646. doi: 10.1093/hmg/6.10.1639 PMID: 9300655

6. Berridge MJ (2010) Calcium hypothesis of Alzheimer?s disease. Pflügers Archiv-European Journal of Physiology 459: 441–449. doi: 10.1007/s00424-009-0736-1 PMID: 19795132

7. Demuro A, Parker I, Stutzmann GE (2010) Calcium signaling and amyloid toxicity in Alzheimer disease. Journal of Biological Chemistry 285: 12463–12468. doi: 10.1074/jbc.R109.080895 PMID: 20212036

8. Bezprozvanny I, Mattson MP (2008) Neuronal calcium mishandling and the pathogenesis of Alzheimer's disease. Trends in Neurosciences 31: 454–463. doi: 10.1016/j.tins.2008.06.005 PMID: 18675468

9. Popugaeva E, Supnet C, Bezprozvanny I (2012) Presenilins, deranged calcium homeostasis, synaptic loss and dysfunction in Alzheimer's disease. Messenger 1: 53–62. doi: 10.1166/msr.2012.1002

10. Green KN, Demuro A, Akbari Y, Hitt BD, Smith IF, et al. (2008) Serca pump activity is physiologically regulated by presenilin and regulates amyloid β production. The Journal of Cell Biology 181: 1107–1116. doi: 10.1083/jcb.200706171 PMID: 18591429

11. Tu H, Nelson O, Bezprozvanny A, Wang Z, Lee SF, et al. (2006) Presenilins Form ER Ca^{2+} Leak Channels, a Function Disrupted by Familial Alzheimer's Disease-Linked Mutations. Cell 126: 981–993. doi: 10.1016/j.cell.2006.06.059 PMID: 16959576

12. Leissring MA, Paul BA, Parker I, Cotman CW, LaFerla FM (1999) Alzheimer's Presenilin-1 Mutation Potentiates Inositol 1, 4, 5-Trisphosphate-Mediated Calcium Signaling in Xenopus. Journal of Neurochemistry 72: 1061–1068.

13. Stutzmann GE (2005) Calcium dysregulation, IP$_3$ signaling, and Alzheimer?s disease. The Neuroscientist 11: 110–115. doi: 10.1177/1073858404270899 PMID: 15746379

14. Cheung KH, Shineman D, Müller M, Cardenas C, Mei L, et al. (2008) Mechanism of Ca^{2+} Disruption in Alzheimer's Disease by Presenilin Regulation of IP$_3$ Receptor Channel Gating. Neuron 58: 871–883. doi: 10.1016/j.neuron.2008.04.015 PMID: 18579078

15. Cheung KH, Mei L, Mak DOD, Hayashi I, Iwatsubo T, et al. (2010) Gain-of-function enhancement of IP$_3$ receptor modal gating by familial Alzheimer's disease-linked presenilin mutants in human cells and mouse neurons. Science Signaling 3: ra22. doi: 10.1126/scisignal.2000818 PMID: 20332427

16. Foskett JK, White C, Cheung KH, Mak DOD (2007) Inositol trisphosphate receptor Ca^{2+} release channels. Physiological Reviews 87: 593–658. doi: 10.1152/physrev.00035.2006 PMID: 17429043

17. Hirashima N, Etcheberrigaray R, Bergamaschi S, Racchi M, Battaini F, et al. (1996) Calcium responses in human fibroblasts: a diagnostic molecular profile for Alzheimer's disease. Neurobiology of aging 17: 549–555. doi: 10.1016/0197-4580(96)00074-7 PMID: 8832629

18. Guo Q, Fu W, Sopher BL, Miller MW, Ware CB, et al. (1999) Increased vulnerability of hippocampal neurons to excitotoxic necrosis in presenilin-1 mutant knock-in mice. Nature Medicine 5: 101–106. doi: 10.1038/4789 PMID: 9883847

19. Oddo S, Caccamo A, Shepherd JD, Murphy MP, Golde TE, et al. (2003) Triple-transgenic model of Alzheimer's disease with plaques and tangles: intracellular Aβ and synaptic dysfunction. Neuron 39: 409–421. doi: 10.1016/S0896-6273(03)00434-3 PMID: 12895417

20. Shilling D, Müller M, Takano H, Mak DOD, Abel T, et al. (2014) Suppression of IP$_3$ Receptor-Mediated Ca^{2+} Signaling Alleviates Mutant Presenilin-Linked Familial Alzheimer's Disease Pathogenesis. J Neurosci 34: 6910–6923. doi: 10.1523/JNEUROSCI.5441-13.2014 PMID: 24828645

21. Ionescu L, White C, Cheung KH, Shuai J, Parker I, et al. (2007) Mode switching is the major mechanism of ligand regulation of IP$_3$R Ca^{2+} release channels. J Gen Physiol 130: 631–645. doi: 10.1085/jgp.200709859 PMID: 17998395

22. Ullah G, Mak DOD, Pearson JE (2012) A data-driven model of a modal gated ion channel: The inositol 1, 4, 5-trisphosphate receptor in insect Sf9 cells. J Gen Physiol 140: 159–173. doi: 10.1085/jgp.201110753 PMID: 22851676

23. Ionescu L, Cheung KH, Vais H, Mak DOD, White C, et al. (2006) Graded recruitment and inactivation of single IP$_3$R Ca^{2+}-release channels: implications for quartal Ca^{2+} release. J Physiol 573: 645–662. doi: 10.1113/jphysiol.2006.109504 PMID: 16644799

24. Mak DOD, Vais H, Cheung KH, Foskett JK (2013) Isolating nuclei from cultured cells for patch-clamp electrophysiology of intracellular ca2+ channels. Cold Spring Harbor protocols 2013: 880. doi: 10.1101/pdb.prot073056 PMID: 24003193

25. Qin F, Auerbach A, Sachs F (2000) Hidden markov modeling for single channel kinetics with filtering and correlated noise. Biophysical Journal 79: 1928–1944. doi: 10.1016/S0006-3495(00)76442-3 PMID: 11023898

26. Qin F, Auerbach A, Sachs F (2000) A direct optimization approach to hidden markov modeling for single channel kinetics. Biophysical Journal 79: 1915–1927. doi: 10.1016/S0006-3495(00)76441-1 PMID: 11023897

27. Magleby K, Pallotta B (1983) Burst kinetics of single calcium-activated potassium channels in cultured rat muscle. The Journal of Physiology 344: 605–623.

28. Ullah G, Parker I, Mak DOD, Pearson JE (2012) Multi-scale data-driven modeling and observation of calcium puffs. Cell calcium 52: 152–160. doi: 10.1016/j.ceca.2012.04.018 PMID: 22682010

29. Ullah G, Bruno WJ, Pearson JE (2012) Simplification of reversible markov chains by removal of states with low equilibrium occupancy. Journal of theoretical biology 311: 117. doi: 10.1016/j.jtbi.2012.07.007 PMID: 22820127

30. Qin F, Auerbach A, Sachs F (1997) Maximum likelihood estimation of aggregated markov processes. Proc Roy Soc Lon Ser B Biol Sci 264: 375–383. doi: 10.1098/rspb.1997.0054

31. Bruno W, Yang J, Pearson J (2005) Using independent open-to-closed transitions to simplify aggregated Markov models of ion channel gating kinetics. Proc Natl Aca Sci USA 102: 6326–6331. doi: 10.1073/pnas.0409110102

32. Colquhoun D, Hawkes AG (1981) Stochastic properties of single ion channels. Philos Trans R Soc Lond B Biol Sci 211: 205–236. doi: 10.1098/rspb.1981.0003

33. Fredkin DR, Montal M, Rice JA (1985) Identification of aggregated Markovian models: application to the nicotinic acetycholine receptor. In: Le Cam LM, Olshen RA, editors, Proceedings of the Berkeley Conference in Honor of Jerzy Neyman and Jack Kiefer. Belmont: Wadsworth Press, pp. 269–289.

34. Shuai J, Pearson J, Foskett J, Mak D, Parker I (2007) A kinetic model of single and clustered IP$_3$R$_s$ in the absence of Ca^{2+} feedback. Biophys J 93: 1151–1162. doi: 10.1529/biophysj.107.108795 PMID: 17526578

35. Leissring MA, Parker I, LaFerla FM (1999) Presenilin-2 mutations modulate amplitude and kinetics of inositol 1, 4, 5-trisphosphate-mediated calcium signals. Journal of Biological Chemistry 274: 32535–32538. doi: 10.1074/jbc.274.46.32535 PMID: 10551803

36. Mullane K, Williams M (2013) Alzheimer's therapeutics: continued clinical failures question the validity of the amyloid hypothesis?but what lies beyond? Biochemical Pharmacology 85: 289–305. doi: 10.1016/j.bcp.2012.11.014 PMID: 23178653

37. LaFerla FM, Green KN, Oddo S (2007) Intracellular Aβ in Alzheimer's disease. Nature Reviews Neuroscience 8: 499–509. doi: 10.1038/nrn2168 PMID: 17551515

38. Mak DOD, Pearson JE, Loong KPC, Datta S, Fernandez-Mongil M, et al. (2007) Rapid ligand-regulated gating kinetics of single IP$_3$R Ca^{2+} release channels. EMBO Reports 8: 1044–1051. doi: 10.1038/sj.embor.7401087 PMID: 17932510

39. Shtifman A, Ward CW, Laver DR, Bannister ML, Lopez JR, et al. (2010) Amyloid-β protein impairs Ca^{2+} release and contractility in skeletal muscle. Neurobiology of Aging 31: 2080–2090. doi: 10.1016/j.neurobiolaging.2008.11.003 PMID: 19108934

40. Palop JJ, Jones B, Kekonius L, Chin J, Yu GQ, et al. (2003) Neuronal depletion of calcium-dependent proteins in the dentate gyrus is tightly linked to Alzheimer's disease-related cognitive deficits. Proceedings of the National Academy of Sciences 100: 9572–9577. doi: 10.1073/pnas.1133381100

41. Kook S, Jeong H, Kang M, Park R, Shin H, et al. (2014) Crucial role of calbindin-D28k in the pathogenesis of Alzheimer?s disease mouse model. Cell Death & Differentiation. doi: 10.1038/cdd.2014.67

42. Lopez JR, Lyckman A, Oddo S, LaFerla FM, Querfurth HW, et al. (2008) Increased intraneuronal resting Ca^{2+} in adult Alzheimer?s disease mice. Journal of Neurochemistry 105: 262–271. doi: 10.1111/j.1471-4159.2007.05135.x PMID: 18021291